Journal of the Meteorological Society of Japan, Vol. 76, No. 4, pp. 561–580, 1998

Low-Frequency Variations and Optimal Excitation in a Simple Barotropic Model with Zonal Asymmetry

By Shozo Yamane[1] and Shigeo Yoden

Department of Geophysics, Kyoto University, Kyoto 606-8502, Japan

(Manuscript received 1 September 1997, in revised form 12 May 1998)

Abstract

Fundamental dynamics of extra-tropical low-frequency variations were investigated by numerical experiments based on a simple spherical barotropic model with forcing, dissipation and topography. Nonperiodic solutions that show low-frequency variations were obtained for realistic parameter ranges. The time average of the solutions has a zonally varying jet structure under the influence of the topography, as the climatological mean state has in the upper troposphere. Some disturbances, which are defined as a deviation from the time average, grew rapidly in a favorable area of upstream and equatorward of the jet maximum. Linear characteristics of the time-averaged basic states, such as eigenmodes, optimal modes, and linear responses of isolated initial perturbations, were examined in detail and were compared with the rapidly growing disturbances in the nonlinear nonperiodic solutions; the rapid growth is explained well by the linear evolution of optimal modes rather than that of unstable eigenmode. The wave activity diagnostics reveal the importance of the propagation of Rossby waves in the zonally varying basic state to the growth of disturbances around the jet exit region.

1. Introduction

The existence of low-frequency variations with time scales longer than that of daily weather disturbances has been recognized in the extra-tropical atmospheric circulations based on upper-air observations. Teleconnection patterns, such as the "Pacific-North American" (PNA) pattern and "East Atlantic" (EA) pattern, are typical examples of the extra-tropical low-frequency variations in the wintertime Northern Hemisphere. They are characterized by geographically fixed, nearly equivalent barotropic structure. Although several theories have been proposed on the physical mechanism of the low-frequency variations, there is no fully satisfactory theory.

Many of the studies on the extra-tropical low-frequency variations have been made based on the barotropic vorticity equation linearized about a zonally varying basic state, which is either an observed time-averaged state in the upper troposphere or an idealized hypothetical state. Some validity of this framework is given, for example, by Simmons *et al.* (1983); they examined linear responses either to localized forcings or to isolated initial perturbations with a global barotropic model linearized about the 300 hPa climatology of geopotential height in January, and showed that structures that resemble the observed PNA and EA patterns tend to recur in both responses. They suggested that the most unstable eigenmode, which is associated with barotropic instability of the zonally varying climatological state, is closely related with the observed teleconnection patterns. However, some room for further investigation is still left in the study of such barotropic instability; Andrews (1984) pointed out that the stability of a zonally varying basic state depends not only on the configuration of the flow but also on the mechanisms that maintain the basic state, such as topography.

About a decade ago, the existence of optimal modes that grow more rapidly than the most unstable eigenmode for a finite time interval was pointed out by Farrell (1988, 1989) and Lacarra and Talagrand (1988). Since then, traditional atmospheric instability problems have been reexamined (*e.g.*, Mukougawa and Ikeda, 1994). The new concept of the optimal modes has also been applied for barotropic zonally varying basic states to study the observed low-frequency variations. Borges and Hartmann (1992) examined the optimal modes of

---

[1] Corresponding author: Shozo Yamane, Frontier Research System for Global Change, SEAVANS North 7F, 1-2-1 Shibaura, Minato-ku, Tokyo 105-6791, Japan.

observed time-mean flows and discussed the importance of the optimal modes in the low-frequency variations. Recently, in a series papers, Borges and Sardeshmukh (1995), Sardeshmukh *et al.* (1997), and Newman *et al.* (1997) pointed out that the growth of both the eigenmode and the optimal mode is too weak to explain the dominant structures of the observed variations and emphasized the importance of the forcing that maintains the basic states. On the other hand, Branstator and Held (1995) showed that the structure and the period of the unstable eigenmodes are similar to those of the large-scale westward propagating disturbances observed recurrently in the wintertime upper troposphere. This is supported by Huang and Robinson (1995), who used linear and nonlinear global barotropic models with an idealized zonally asymmetric basic state.

Another category of studies on the extra-tropical low-frequency variations is based on the theory of barotropic Rossby-wave propagation in a zonally varying basic state. Hoskins and Ambrizzi (1993) pointed out the waveguide effect of zonally varying jets on stationary Rossby waves with the WKB theory, and confirmed the effect in the response of a barotropic model linearized about a climatological 300 hPa flow to localized forcing. The propagation of Rossby waves with non-zero frequency was also examined theoretically and numerically by Yang and Hoskins (1996). Naoe *et al.* (1997) studied the linear barotropic response of idealized basic states to a localized vorticity forcing using the wave activity diagnostics introduced by Plumb (1986), and showed that the wave energy tends to increase in the jet exit region. The barotropic modulation of the amplitude and structure of the waves propagated in zonally varying basic states was studied with simple contour-dynamics models by Swanson *et al.* (1997); they showed increase of particle displacement amplitude and increase of zonal wavenumber in the jet exit region using the conservation law of wave activity.

Relation among the theories of growing modes (eigenmodes or optimal modes) and that of Rossby wave propagation in a zonally varying basic state is not fully understood yet, although these theories are based on the same linearized barotropic model. Which linear property of the time-averaged basic states may be related with the extra-tropical low-frequency variations remains an unanswered question. Our purpose with this paper is to clarify the relation among the linear theories on the time-averaged basic states and their relation to the low-frequency variations in the nonperiodic solutions in the same framework of a simplified spherical barotropic model. We examined eigenmodes and optimal modes of the time-averaged basic states, and made the wave activity diagnostics for the Rossby wave propagation in the time-averaged basic state to compare these linear results with the nonperiodic nonlinear solutions. Details of the model are described in Section 2. Section 3 shows the solutions of the nonlinear model, and Section 4 shows the results of the linear analyses with respect to the time-averaged state. Discussion is given in Section 5, and conclusions are given in Section 6.

2. Model

We use a simple atmospheric circulation model that is a modification of the Legras and Ghil (1985, referred to as LG) model. The model is governed by the barotropic vorticity equation on a rotating sphere with forcing, dissipation and surface-topography terms. Its nondimensional form is as follows:

$$\begin{aligned}&\frac{\partial}{\partial t}\varDelta\psi + J[\psi, \rho\varDelta\psi + \mu(1+h)]\\ &\quad = \alpha\varDelta(\psi^* - \psi) - \nu\varDelta^9\psi,\end{aligned} \tag{1}$$

where $\psi(\lambda, \mu, t)$ is the streamfunction, λ the longitude, μ the sine of the latitude: $\mu = \sin\phi$, ϕ the latitude, t the time, $\psi^*(\mu)$ the streamfunction for a zonally symmetric forcing, $h(\lambda, \mu)$ the topographic height, $\varDelta$ the spherical Laplacian operator, J the spherical Jacobian operator, α^{-1} the relaxation time, ν the artificial hyper-diffusion coefficient whose term is added for smooth numerical behavior, and ρ the nondimensional number that corresponds to the Rossby number and measures the intensity of the forced zonal wind $\boldsymbol{u}^* \equiv \rho\left(-\frac{\partial\psi^*}{\partial\phi}, 0\right)$. Without the right-hand side of the equation, the potential vorticity $q \equiv \rho\varDelta\psi + \mu(1+h)$ is conserved following the wind $\boldsymbol{u} \equiv \rho\left(-\frac{\partial\psi}{\partial\phi}, \frac{1}{\cos\phi}\frac{\partial\psi}{\partial\lambda}\right)$, that is, $\left(\frac{\partial}{\partial t} + \boldsymbol{u}\cdot\nabla\right)q = 0$.

Equation (1) is discretized through an expansion in spherical harmonics $P_n^m(\mu)e^{im\lambda}$ with a triangular truncation of total wavenumber 42 (T42): $\psi(\lambda, \mu, t) = \sum_{n=0}^{42}\sum_{m=-n}^{n}\psi_n^m(t)P_n^m(\mu)e^{im\lambda}$, where $P_n^m(\mu)$ are associated Legendre functions normalized to satisfy $\int_{-1}^{1}\{P_n^m(\mu)\}^2 d\mu = 2$. The truncation wavenumber was determined after a preliminary convergence test by changing the wavenumber. Our model corresponds to a dynamical system of 1848 real variables, which is much larger system than the original LG model of 25 real variables.

We use the same forcing as LG, $\psi^*(\mu) = -\kappa\mu^3$, which is a zonal jet with a maximum near the latitude of 50°. The coefficient κ is set to such a constant that the maximum zonal wind is 60 ms^{-1} in dimension for $\rho = 0.2$. Latitudinal profiles of the zonal wind and the potential vorticity of the forcing for $\rho = 0.18$ are shown with a solid line and a dashed line in Fig. 1a, respectively. The topography in the Northern Hemisphere is identical with that given by LG and no topography is assumed in the Southern Hemisphere; $h(\lambda,\mu) = 4h_0\mu^2(1-\mu^2)\cos 2\lambda$ for $\mu \geq 0$ and $h(\lambda,\mu) = 0$ for $\mu < 0$. The amplitude of the topography is set to $h_0 = 0.1$. The spatial structure of the topography is shown in Fig. 1b for the Northern Hemisphere. The relaxation time α^{-1} is set to 10 days in dimension, and the hyper-diffusion coefficient ν is set to give a damping time of 0.5 day at the largest total wavenumber 42. The forcing parameter ρ is changed as an experimental parameter in Subsection 3.1, and fixed to $\rho = 0.18$ in Subsection 3.2 and afterward.

A linearized model of Eq. (1) is also used in this study. The nonlinear model (1) can be written formally as

$$\frac{d}{dt}\boldsymbol{x} = \boldsymbol{f}(\boldsymbol{x}), \tag{2}$$

where $\boldsymbol{x}(t)$ is a vector that consists of the expansion coefficients of streamfunction, $\psi_n^m(t)$. Let $\bar{\boldsymbol{x}}$ be a basic state that is independent of time t, and let $\boldsymbol{x}'(t)$ be a deviation from $\bar{\boldsymbol{x}}$; $\boldsymbol{x}'(t) = \boldsymbol{x}(t) - \bar{\boldsymbol{x}}$. Suppose that $\boldsymbol{x}'$ is small and $\boldsymbol{f}(\bar{\boldsymbol{x}})$ is also small ($\boldsymbol{f}(\bar{\boldsymbol{x}}) = \mathbf{o}$ if $\bar{\boldsymbol{x}}$ is a stationary solution), then we get a linearized equation from Eq. (2):

$$\frac{d}{dt}\boldsymbol{x}' = \mathsf{J}(\bar{\boldsymbol{x}})\boldsymbol{x}', \tag{3}$$

where J is Jacobian matrix $J_{ij} = \partial f_i/\partial x_j$. In this study, the linearized barotropic model of Eq. (3) is also used for a time-averaged solution $\bar{\boldsymbol{x}}$. Note that the topographic term that maintains the zonally varying basic state is retained in the linearized model except that otherwise mentioned.

3. Nonlinear solutions

3.1 Bifurcation diagram

To understand the dynamical structure of the nonlinear barotropic model, stationary solutions and asymptotic solutions were computed for some parameter range of ρ and bifurcation diagrams were constructed. The stationary solutions were obtained by the continuation method, details of which were described by Kubiček and Marek (1983) and LG, and their linear stability was given by solving an eigenvalue problem of the linearized Eq. (3). Figure 2 shows the dependence of the stationary solutions on ρ, whose linear stability is represented by the type of markers for two expansion coefficients of the streamfunction: (a) a real part of ψ_3^2, which is one of the expansion coefficients with even zonal wavenumber (EVENs), and (b) a real part of ψ_2^1, which is one of the expansion coefficients with odd zonal wavenumber (ODDs). The external condition of the present model has a longitudinal periodicity

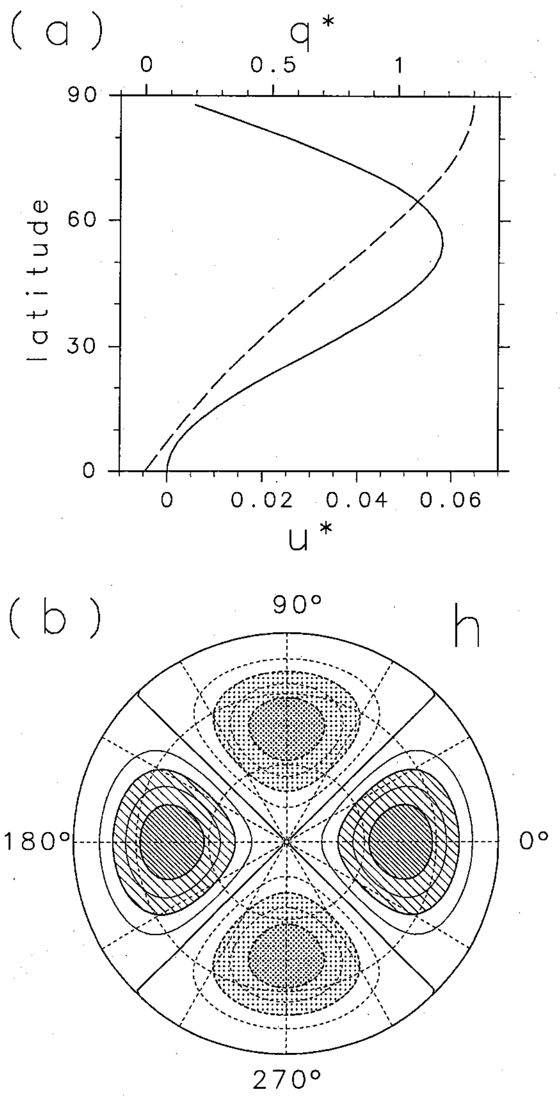

Fig. 1. (a) Latitudinal profiles of the nondimensional zonal wind u^* (solid line) and potential vorticity q^* (dashed line) of the forcing for $\rho = 0.18$. The maximum of u^* is 54 ms^{-1} in dimension. (b) Contour map of the topography $h(\lambda,\mu)$ in the Northern Hemisphere with Lambert's azimuthal equal-area projection. The center of the map is the North Pole, the outer circle is the equator, the meridian on the right side is $\lambda = 0$, and meridians and parallels are drawn every 30°. Solid contours are positive or zero and dashed contours are negative. Contour interval is 0.02 and shading indicates the region greater than 0.04 or less than −0.04. The same projection is used in the successive spherical maps except for Fig. 17.

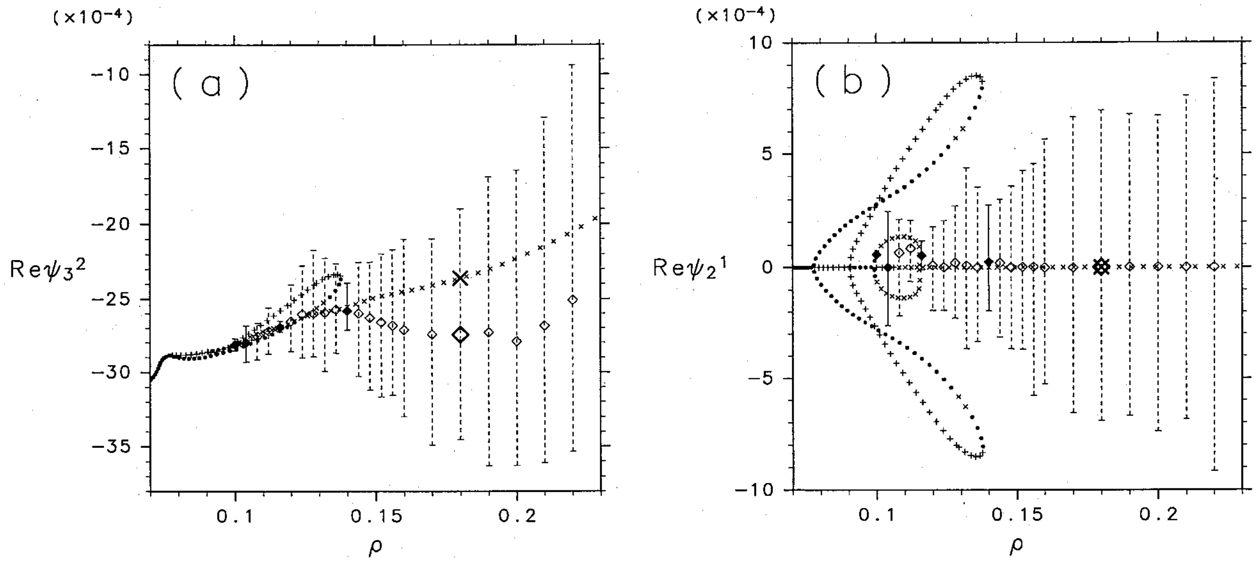

Fig. 2. Dependence of stationary solutions and asymptotic solutions on the forcing parameter ρ for two expansion coefficients of the streamfunction: (a) real part of ψ_3^2 and (b) real part of ψ_2^1. Linear stability of the stationary solutions is represented by the following markers: • stable, + unstable (the eigenvalue with the largest real part is real), and × unstable (the eigenvalue with the largest real part is complex). Time average and variable range of the asymptotic solutions are indicated by diamonds and vertical lines, respectively; a closed diamond and solid line represent a periodic solution and an open diamond and dashed line represent a chaotic solution.

of mod π, because the forcing ψ^* is limited to zonal components ($m = 0$) and the topography consists only of $m = 2$ components. Hence, a branch of stationary solutions whose ODDs are all equal to zero may exist, and actually such a branch does exist on the zero-line in Fig. 2b. We call it the main branch hereafter.

Stationary solutions of the main branch are stable when ρ is small ($\rho < 0.077$). At $\rho = 0.077$, the main branch loses stability and two new stable branches with non-zero ODDs of opposite sign appear as a super-critical bifurcation. The main branch becomes stable again at $\rho = 0.091$, where the two unstable branches appear as a sub-critical bifurcation, each of which is connected with the previous stable branch with ODDs. Another super-critical bifurcation occurs again at $\rho = 0.099$, and the solutions of the main branch remain unstable for $\rho > 0.099$, although the new branches merge the main branch again at $\rho = 0.115$. The multiplicity of stable stationary solutions is observed almost in the range of $0.077 < \rho < 0.138$. However, it does not correspond to the multiple stable states that Charney and DeVore (1979) obtained as a result of the nonlinear resonance of topographically forced Rossby waves; in their case, both stable solutions have the same zonal wave number as the topography, while non-zero ODDs are also required for the multiplicity in the present case.

Asymptotic behavior of time-dependent solutions is obtained by numerical time integrations with the fourth-order Runge-Kutta method, starting from an initial condition close to $\psi = 0$. Time average and variable range of the asymptotic solutions are shown in Fig. 2 for the parameter range of $0.100 \leq \rho \leq 0.220$, where the stationary solutions of the main branch are unstable. The time average and variable range of periodic solutions are indicated by a closed diamond and solid line, respectively, while those of chaotic solutions are indicated by an open diamond and dashed line. Some of the asymptotic solutions have a symmetric character of ODDs due to the longitudinal periodicity of mod π, while others do not have such symmetry with non-zero time average of ODDs. In the former (symmetric) case, the solution with opposite sign of ODDs is identical to that solution with a phase lag of π in λ, while in the latter (unsymmetric) case, there exist a couple of asymmetric solutions with opposite sign of ODDs.

In the parameter range of $0.100 \leq \rho \leq 0.140$, the asymptotic solutions are full of variety; periodic solutions are observed frequently among chaotic solutions just like periodic windows. In Fig. 2b the periodic solution for $\rho = 0.104$ is symmetric while those for $\rho = 0.100$, 0.116, and 0.140 are unsymmetric. Nearby chaotic solutions often show the temporal variation which is very similar to that of these periodic solutions.

Figure 3 shows the temporal variation and the power spectral density of Re$[\psi_2^1(t)]$ for the asymptotic solutions in the parameter range of $0.140 \leq \rho \leq 0.220$. The solution for $\rho = 0.14$ (a) is an un-

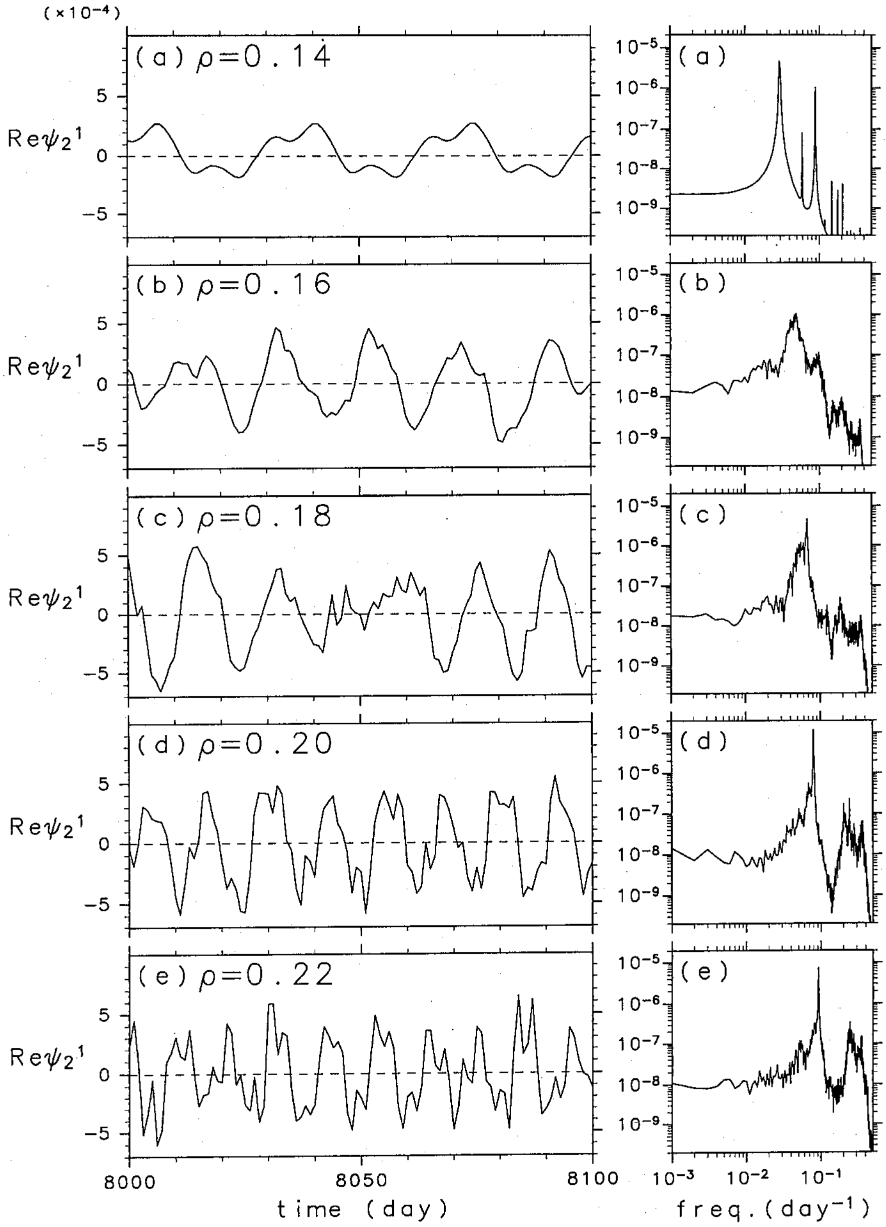

Fig. 3. Temporal variation and power spectral density of real part of $\psi_2^1(t)$ for the asymptotic solutions. The forcing parameter ρ is, respectively, (a) 0.14, (b) 0.16, (c) 0.18, (d) 0.20, and (e) 0.22. The power spectral density, based on the 10,000-day dataset, shows a power peak at the period of (a) 34.5 days, (b) 20.4 days, (c) 14.7 days, (d) 12.3 days, and (e) 10.9 days, respectively.

symmetric periodic solution with a period of about 35 days, while the others for $\rho \geq 0.16$ (b–e) are chaotic solutions with a strong peak of the period of $10 \sim 20$ days, which becomes shorter as ρ increases. The high-frequency components, less than 5 days, have more power with ρ.

In the following section, we shall focus on the case with a parameter value of $\rho = 0.18$ as a typical example of the chaotic solutions with low-frequency variability, and investigate the relation between the temporal variation of the chaotic solution and inherent properties of the time-averaged state.

3.2 Stationary solution and time-averaged state for $\rho = 0.18$

The streamfunction ψ_s and the potential vorticity q_s of the stationary solution for $\rho = 0.18$, which belongs to the main branch and is shown with a thick marker × in Fig. 2, are shown in Figs. 4a and 4b, respectively, for the Northern Hemisphere. Here, subscript s represents the stationary solution. Those for the Southern Hemisphere are close to the zonal forcing, ψ^* and $\rho\Delta\psi^* + \mu$. The longitudinal periodicity of mod π is recognized in Figs. 4a and 4b, as mentioned in the previous subsection. Troughs of ψ_s are

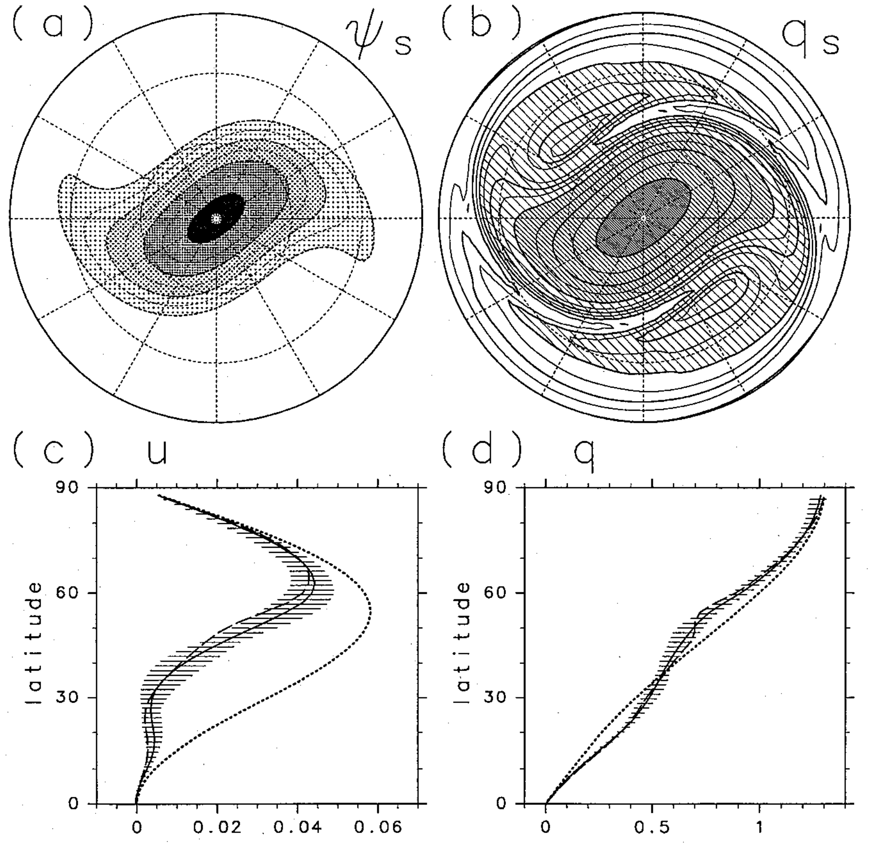

Fig. 4. Contour maps of (a) the streamfunction ψ_s and (b) the potential vorticity q_s of the stationary solution for $\rho = 0.18$. Contour interval is, respectively, (a) 0.02, and (b) 0.1. Shading indicates the region (a) less than -0.04, and (b) greater than 0.4. Latitudinal profiles of (c) the zonal mean zonal wind and (d) the zonal mean potential vorticity for the stationary solution (dashed lines) and the time-averaged state (solid lines). Horizontal lines show the range of the temporal variation for the asymptotic solution. Dotted lines indicate the profiles of the forcing, which are identical with those shown in Fig. 1a.

seen about 30° eastward relative to the top of topography at 60°N and are tilted northeast-southwest direction; troughs are about on the top of topography at 30°N. The potential vorticity q_s has a similar distribution as ψ_s in high latitudes with opposite sign (*i.e.*, positive in the Northern Hemisphere), and it has two secondary maxima near points of $(\lambda, \phi) = (130°, 45°\mathrm{N})$ and $(\lambda, \phi) = (310°, 45°\mathrm{N})$. Two areas that satisfy the inequality $\partial q_s/\partial\phi < 0$ exist along lines from $(0°, 10°\mathrm{N})$ to $(150°, 50°\mathrm{N})$ and from $(180°, 10°\mathrm{N})$ to $(330°, 50°\mathrm{N})$. These areas are considered to be locally unstable because the necessary condition for the barotropic instability is satisfied locally.

Traditional linear stability of the stationary solution is examined by computing eigenvalues and eigenvectors (, or eigenmodes) of Jacobian matrix of Eq. (3), which is linearized with respect to the stationary solution. It is unstable because five pairs of complex eigenvalues have a positive real part; the e-folding time (T_e) and the period (T_p) corresponding to each pair are listed in Table 1. The eigenmode associated with the pair of the most unstable complex eigenvalues, of which the e-folding time is 7.8 days, has substantial variations in the limited ar-

Table 1. Characteristics of unstable eigenmodes. The e-folding time T_e and the period T_p, which correspond to the pairs of complex eigenvalues with positive real part of Jacobian matrix of Eq. (3), are listed for three basic states of the stationary solution ψ_s, the time-averaged state $\bar{\psi}$, and the time-averaged state $\bar{\psi}$ without the topographic term for $\rho = 0.18$.

	T_e (day)	T_p (day)
ψ_s	7.8	5.6
	8.1	4.1
	8.7	12.7
	12.7	7.4
	18.8	3.6
$\bar{\psi}$	17.3	15.7
$\bar{\psi}$ (no topo)	30.5 46.0	15.5 10.1

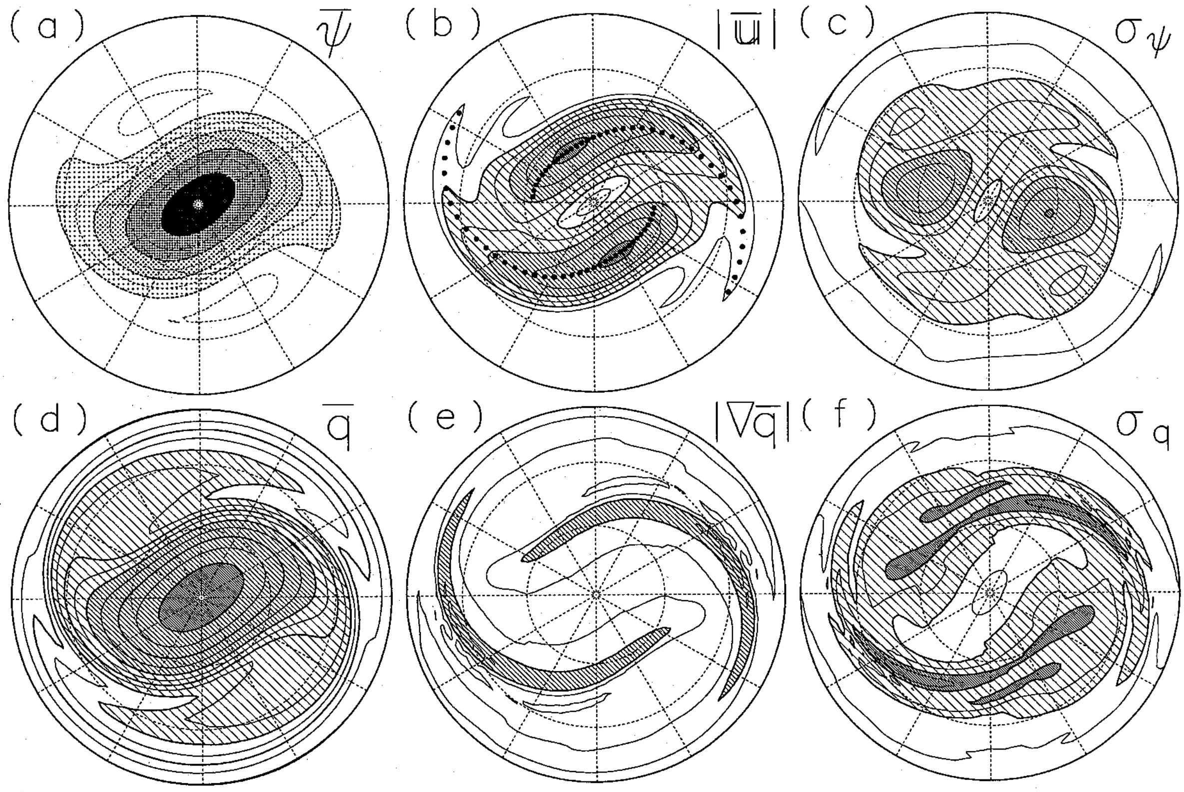

Fig. 5. Statistics of the asymptotic solution for $\rho = 0.18$ based on the 10,000-day dataset. The time-averaged field is represented by (a) streamfunction $\bar{\psi}$, (b) wind speed $|\bar{u}|$, (d) potential vorticity $\bar{q}$, and (e) absolute value of potential vorticity gradient $|\nabla\bar{q}|$. The temporal variation is summarized by (c) the standard deviation of streamfunction σ_ψ and (f) that of potential vorticity σ_q. Dots in (b) indicate two jets as the line of $\partial|\bar{u}|/\partial\phi = 0$. Contour interval is, respectively, (a) 0.02, (b) 0.01, (c) 0.002, (d) 0.1, (e) 1, and (f) 0.02. Shading indicates the region (a) < -0.04, (b) > 0.02, (c) > 0.004, (d) > 0.4, (e) > 2, and (f) > 0.04.

eas of (90–180°, 30–60°N) and (270–360°, 30–60°N), where $\partial q_s/\partial\phi < 0$. The other three eigenmodes associated with the pairs whose period is less than 10 days also have similar characteristics. The eigenmode of the third pair with a period of 12.7 days is not localized very much and shows similar temporal variation to that of the unstable eigenmode of the time-averaged state, of which the evolution will be shown later in Fig. 10.

We will describe statistics of the chaotic solution for $\rho = 0.18$ based on a 10,000-day dataset. Figure 4c shows latitudinal profiles of the zonal mean zonal wind for the stationary solution (dashed line) and for the time-averaged state (solid line) together with the range of the temporal variation (horizontal lines). The profiles of the stationary solution and the time average are very similar. Compared with the profile of the forcing (dotted line), these mean zonal flows are reduced largely in the latitudes of 30–60°N, where the topographic amplitude is large. Large temporal variations of about 10 ms^{-1} are seen around $\phi = 40$°N and 60°N. Latitudinal profiles of the potential vorticity are also shown in Fig. 4d in the same manner as the zonal wind in Fig. 4c. The profile of zonal mean potential vorticity $[q_s]$ implies the barotropic instability near $\phi = 50$°N, where the condition $d[q_s]/d\phi < 0$ is satisfied. Here, square brackets represent the zonal mean. The instability is considered to be induced by the effect of topography, because the zonal forcing itself is barotropically stable as the dotted line (or the dashed line in Fig. 1a) shows. The profile of the time mean $[\bar{q}]$ shows a monotonic increase with latitude, indicating the disappearance of the unstable zone due to the vorticity mixing. Here, the over bar represents the time average.

Figures 5a and 5d show the time averages of the streamfunction $\bar{\psi}$ and the potential vorticity $\bar{q}$. These fields almost show the longitudinal periodicity of mod π, and the large-scale structure is similar to that of the stationary solution shown in Figs. 4a and 4b. However, the negative gradient of the potential vorticity along the lines from (0°, 10°N) to (150°, 50°N) and from (180°, 10°N) to (330°, 50°N) seen in q_s is weakened in the time-averaged field, because the potential vorticity is

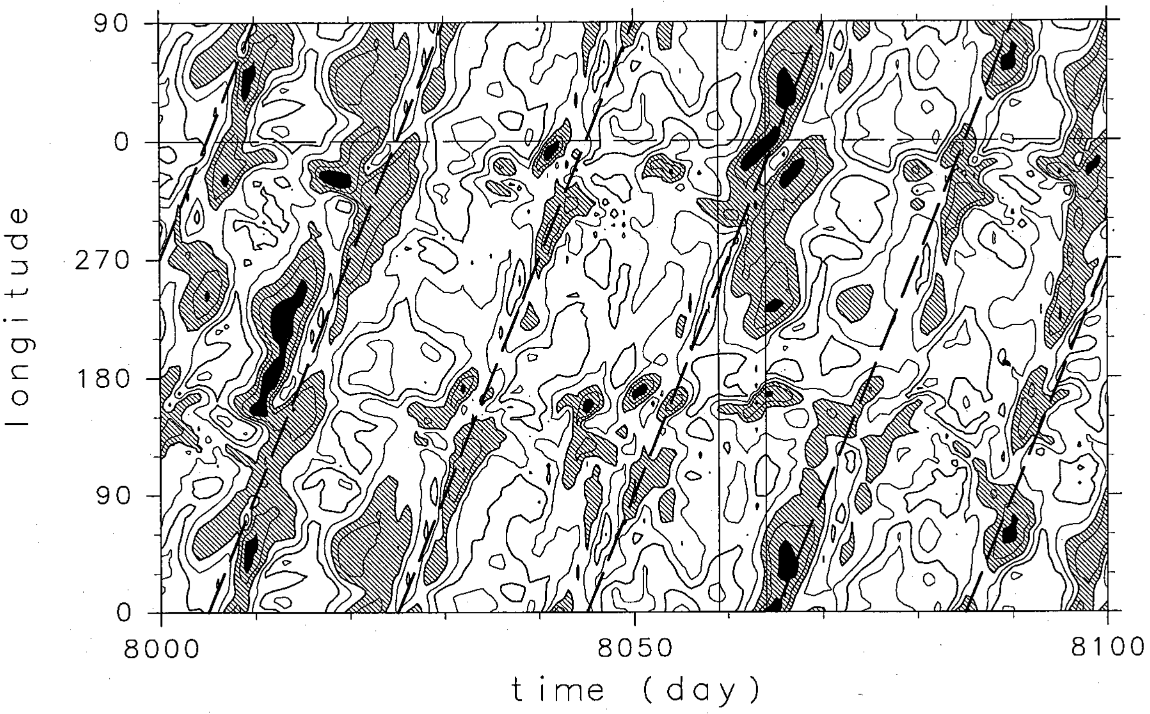

Fig. 6. Hovmöller diagram of the vorticity disturbance with a quantity $\{q'^2\}^{1/2}$, which is a square root of q'^2 averaged over latitudes of $\phi = 29.3$–$60.0°$N. A thin dashed line shows one cycle of the longitude. Thick dashed lines show a phase speed of 18° day^{-1}. Contour interval is 0.02 and shading indicates the region greater than 0.08. The period of Day 8059–8064 is indicated by two vertical solid lines.

well-mixed by the disturbances that are repeatedly developed in these locally unstable areas. Figure 5b shows the spatial distribution of the wind speed $|\bar{u}|$, which shows two jets denoted by dots as the line of $\partial|\bar{u}|/\partial\phi = 0$. The latitude of the jets shifts poleward with longitude. The jet reaches a maximum speed of about 57 ms^{-1} in dimension at $(115°, 65°\mathrm{N})$ and $(295°, 65°\mathrm{N})$, which exceeds the maximum of the forced zonal wind (54 ms^{-1}) a little. Figure 5e shows the absolute value of the gradient of potential vorticity $|\nabla\bar{q}|$. Shaded areas of large $|\nabla\bar{q}|$, which are considered to be a waveguide of Rossby waves, are seen just to the south of the jets.

Figure 5c shows the spatial distribution of the standard deviation of the streamfunction, σ_ψ. The areas of large σ_ψ are located in the jet exit regions around $(170°, 60°\mathrm{N})$ and $(350°, 60°\mathrm{N})$. Figure 5f also shows the standard deviation of the potential vorticity, σ_q. The dark-shaded areas of large σ_q are seen both in the areas of large $|\nabla\bar{q}|$ shaded in Fig. 5e and in the areas where a large difference between q_s and $\bar{q}$ is recognized. The former seems to be related to the propagation of Rossby waves along the waveguide, while the latter seems to be related to the development of barotropically unstable disturbances.

In the Southern Hemisphere, the time mean $\bar{\psi}$ is nearly the same as the zonal forcing ψ^* and the temporal variation is much smaller than that in the Northern Hemisphere.

3.3 Details of the temporal variability for $\rho = 0.18$

Temporal variations of the chaotic solution for $\rho = 0.18$ are investigated by using vorticity disturbance $q'(\lambda, \mu, t)$, which is the deviation of $q(\lambda, \mu, t)$ from $\bar{q}(\lambda, \mu)$. To see the longitudinal propagation of the disturbance, a Hovmöller diagram is made using a quantity $\{q'^2\}^{1/2}$, which is a square root of q'^2 averaged over latitudes of $\phi = 29.3$–$60.0°$N, where large variations of the vorticity are seen in Fig. 5f. Figure 6 shows the diagram for the period of Day 8000–8100. Most of large-amplitude disturbances propagate eastward with a phase speed of about 18° day^{-1} (thick dashed lines). Such propagating disturbances are active in some periods, *e.g.*, around Day 8010 and 8065, while they are not in Day 8030–8060.

To quantify the growth of the disturbances we introduce a global measure $\|q'\|$, which is a square root of q'^2 averaged over the globe: $\|q'\| = \langle q', q'\rangle^{\frac{1}{2}}$ where $\langle\alpha, \beta\rangle \equiv \dfrac{1}{4\pi}\displaystyle\int_0^{2\pi}\int_{-1}^{1} \alpha\beta d\mu d\lambda$. That is, $\|q'\|$ represents the magnitude of the disturbance q' based on the enstrophy norm. A thick solid line in Fig. 7 shows the temporal variation of $\|q'\|$ for the same period as in Fig. 6. Irregular fluctuation of $\|q'\|$ is seen with a rapid growth in the periods of Day 8000–8010 and Day 8060–8065, which are followed

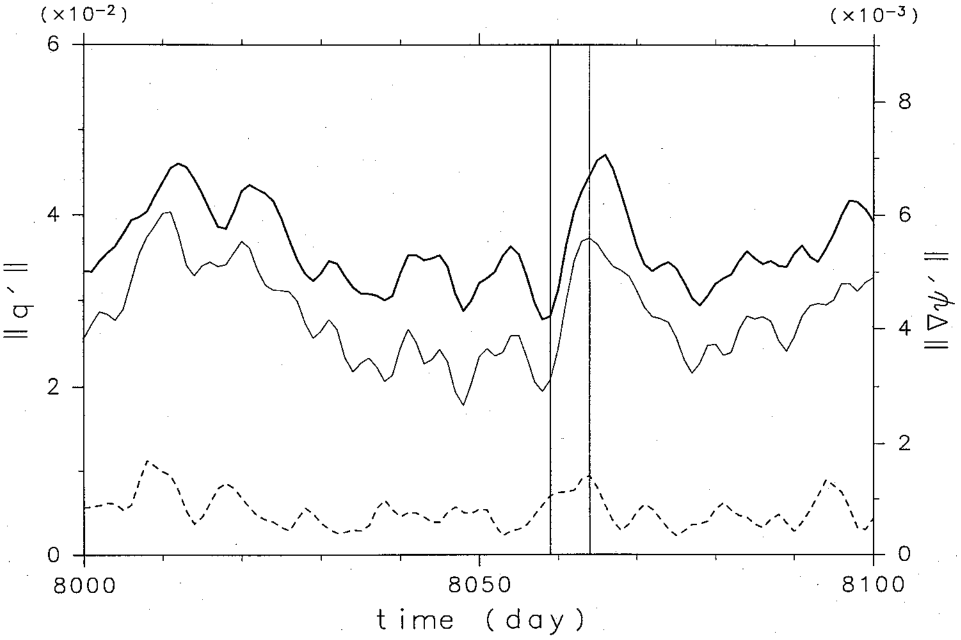

Fig. 7. Temporal variation of the global measure of vorticity disturbance based on the enstrophy norm, $\|q'(t)\|$(thick solid line). A thin solid line shows the global measure of disturbance based on the energy norm, $\|\nabla\psi'(t)\|$. A dashed line shows the global measure of projection of the disturbance $q'(t)$ onto the space spanned by the first 5 optimal modes, whose spatial structures are shown in the upper panels of Fig. 15. Two vertical solid lines show the period of Day 8059–8064.

by the active periods of the disturbances seen in Fig. 6 for mid-latitudes in the Northern Hemisphere. The rapid growth of $\|q'\|$ in the period of Day 8059–8064, which is indicated by two vertical solid lines, is investigated thoroughly to clarify its dynamics. In the 10,000-day dataset such rapid growth is sometimes detected.

A thin solid line in Fig. 7 shows the temporal variation of the magnitude of the disturbance based on the energy norm denoted as $\|\nabla\psi'\|$ for the same period. The fluctuation of $\|\nabla\psi'\|$ (thin solid line) is similar to that of $\|q'\|$ (thick solid line), and a more rapid growth of $\|\nabla\psi'\|$ is also seen in the period indicated by two vertical solid lines.

Figure 8 shows the temporal variations of the potential vorticity q and the wind $\boldsymbol{u}$ for the period of Day 8059–8064. Relatively large changes in the q field are seen in the Western Hemisphere of $180° \leq \lambda \leq 360°$. An air mass of low q around (210°, 30°N) at Day 8059 (a) is advected downstream into higher latitudes to form a low q area in (230–280°, 30–50°N) at Day 8064 (f). An enhanced ridge of q is seen around $\lambda = 260°$ at Day 8061 (c), and advected eastward to reach about 310° at Day 8064 (f), while a trough in high-latitudes is seen around 330° at Day 8061 (c) and advected to reach about 360° at Day 8064 (f). These propagations of ridge and trough are recognized more clearly in the disturbance field of the potential vorticity, q', as shown in Fig. 9. Temporal variation of q described above can be easily identified; the advection of low q (negative q') from low-latitudes to mid-latitudes and the movement of the ridge (positive q') and the trough (negative q') in mid- and high-latitudes. The rapid growth of the global measure $\|q'\|$ shown with the thick solid line in Fig. 7 can be attributed to the growing disturbances in the mid-latitudes, mainly in the Western Hemisphere.

4. Linear analyses

4.1 Eigenmodes of the time-averaged field

We investigated a possible relation between the eigenmodes of the time-averaged field and the vorticity disturbances shown in the previous section. The Jacobian matrix of Eq. (3), which is linearized with respect to the time-averaged state shown in Fig. 5, has a pair of complex eigenvalues with a positive real part. The e-folding time T_e is 17.3 days and the period T_p is 15.7 days for the unstable mode. The period gives a good estimate for the dominant period of the chaotic solution shown in Fig. 3c. Let $a_1(\lambda,\mu)$ and $a_2(\lambda,\mu)$ be two vorticity fields of the associated eigenmode. The linear evolution of the eigenmode vorticity perturbation $\xi(\lambda,\mu,t)$ is generally written in the form

$$\xi(\lambda,\mu,t) = A_0\left\{a_1(\lambda,\mu)\sin\frac{t-t_0}{T_p} + a_2(\lambda,\mu)\cos\frac{t-t_0}{T_p}\right\} \exp\frac{t-t_0}{T_e}. \quad (4)$$

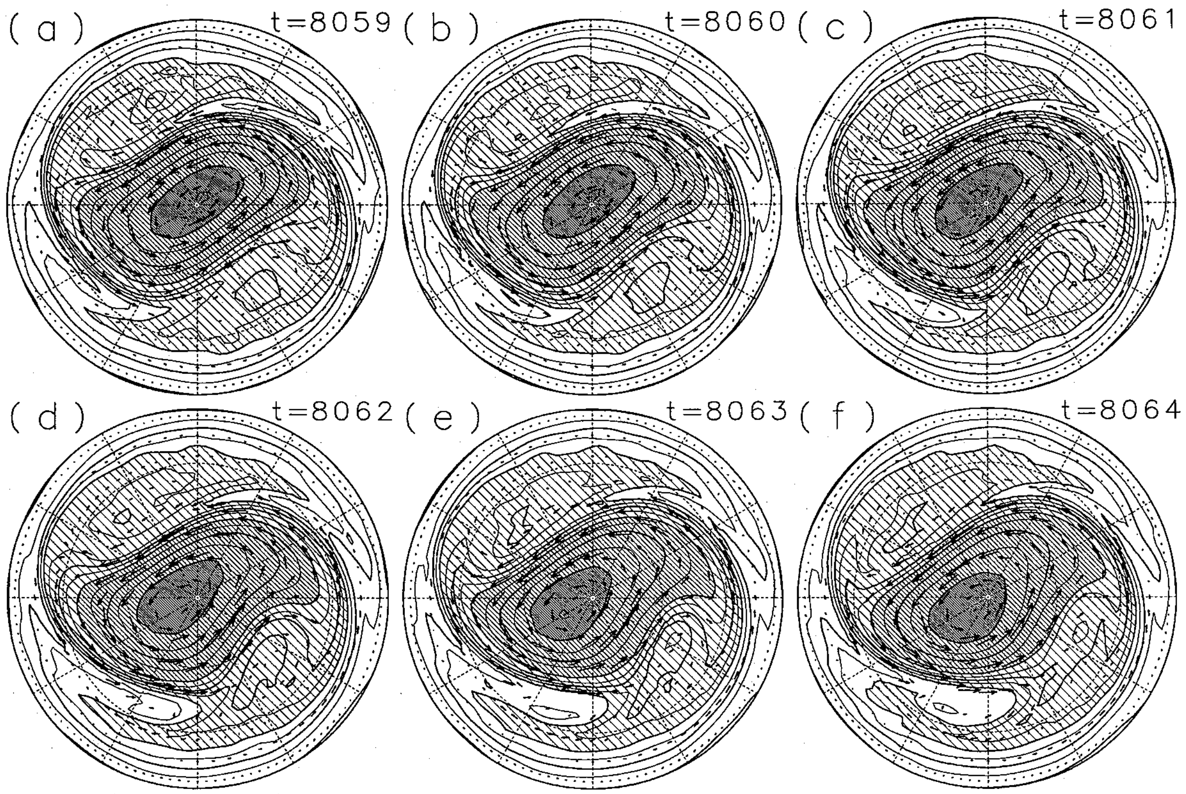

Fig. 8. Contour maps of the potential vorticity $q(t)$ for the period of Day 8059–8064. Contour interval is 0.1 and shading indicates the region greater than 0.4. Arrows show the wind u.

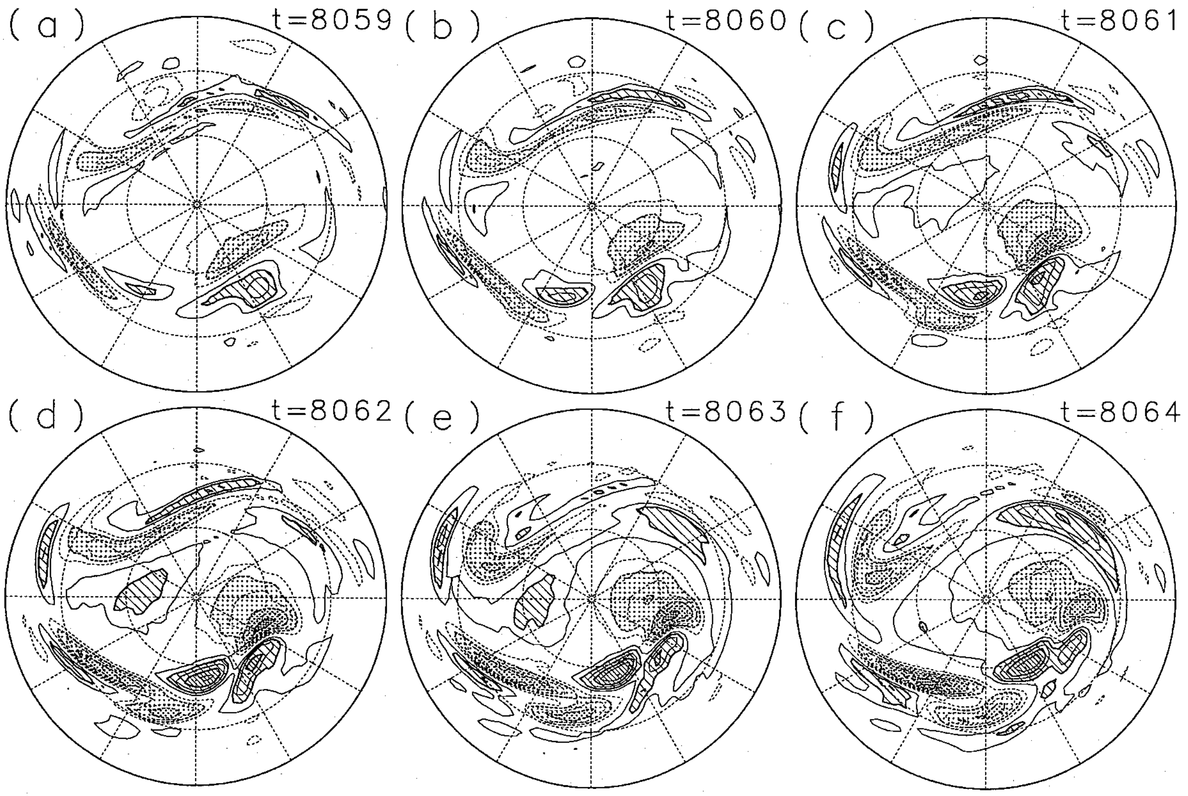

Fig. 9. Contour maps of the vorticity disturbance $q'(t)$ for the same period as that in Fig. 8. Contour interval is 0.04 and shading indicates the region greater than 0.08 or less than -0.08. Zero-contours are omitted.

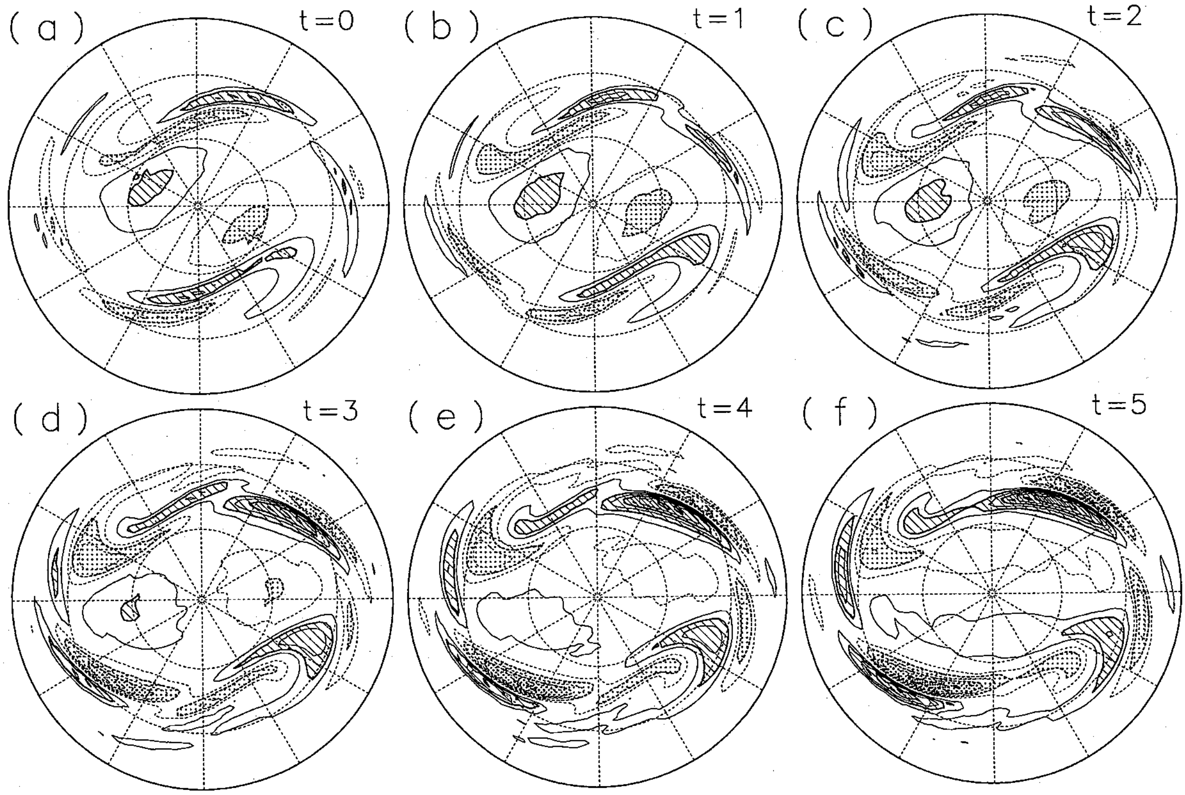

Fig. 10. Linear evolution of the eigenmode vorticity perturbation $\xi(t)$, whose e-folding time and period are 17.3 days and 15.7 days, respectively. Contour interval is 0.02 and shading indicates the region greater than 0.04 or less than -0.04. Zero-contours are omitted.

Now the amplitude A_0 and the phase t_0 of Eq. (4) are determined so as to satisfy $C(q'_{\mathrm{I}}, \xi_0) = \max_{0 \le t < T_p} C(q'_{\mathrm{I}}, \xi(\lambda, \mu, t))$ and $\|\xi_0\| = C(q'_{\mathrm{I}}, \xi_0) \times \|q'_{\mathrm{I}}\|$, where $q'_{\mathrm{I}} \equiv q'(\lambda, \mu, t = \text{Day } 8059)$, $\xi_0 \equiv \xi(\lambda, \mu, t = \text{Day } 0)$, and $C(\alpha, \beta)$ is a coefficient of correlation between α and β: $C(\alpha, \beta) = \dfrac{\langle \alpha, \beta \rangle}{\|\alpha\| \|\beta\|}$. That is, ξ_0 is equal to the orthogonal projection of q'_{I} with respect to the vorticity field onto the plane spanned by $a_1(\lambda, \mu)$ and $a_2(\lambda, \mu)$ in 1848-dimensional phase space.

Figure 10 shows the temporal variation of $\xi(\lambda, \mu, t)$ for the period of Day $0 \le t \le$ Day 5. The unstable eigenmode is nearly antisymmetric with respect to the axis of rotation, *i.e.*, all the EVENs of the eigenmode are nearly zero. In comparison to the evolution of the vorticity disturbance q' in Fig. 9, that of the eigenmode ξ in Fig. 10 shows a very similar variation in the Eastern Hemisphere of $0° \le \lambda \le 180°$. It is consistent with the fact that the coefficient of correlation between q'_{I} and ξ_0 is as much as 0.50. However, in the Western Hemisphere, especially in longitudes of 240–360° where the vorticity disturbance q' shows the rapid growth for the period of Day 8059–8064, a close correspondence between these two evolutions is not observed.

Quantitative comparisons were made between the two evolutions. A solid line in Fig. 11a shows the temporal variation of the global mean enstrophy of the disturbance $\|q'(t)\|^2$ for the period of Day 8056–8069, which is the square of the quantity indicated by the thick solid line in Fig. 7, while a dot-dashed line shows that of the eigenmode vorticity perturbation $\|\xi(t)\|^2$, of which the initial value $\|\xi_0\|^2$ is marked by an open circle at Day 8059. Although the global mean enstrophy of the eigenmode $\|\xi(t)\|^2$ becomes large for this period, the increment of $\|\xi(t)\|^2$ is less than a quarter of the increment of $\|q'(t)\|^2$. A dot-dashed line in Fig. 11b shows the temporal variation of the coefficient of correlation between $q'(t)$ and $\xi(t)$, $C(q'(t), \xi(t - 8059 \text{ days}))$. The coefficient of correlation at $t =$ Day 8059, $C(q'_{\mathrm{I}}, \xi_0)$, is equal to 0.50 (marked by an open circle) and $C(q'(t), \xi(t - 8059 \text{ days}))$ does not change very much for the period of Day 8059–8064. Note that the coefficient of correlation between $q'(t)$ and the linear evolution whose initial value is the whole q'_I decreases monotonously from 1 at Day 8059 to 0.67 at Day 8064. In this model, the unstable eigenmode $\xi(\lambda, \mu, t)$ can not explain the rapid growth of $\|q'(t)\|$ quantitatively, although it seems to represent a fundamental tone that exists in the irregular fluctuation of $q'(t)$.

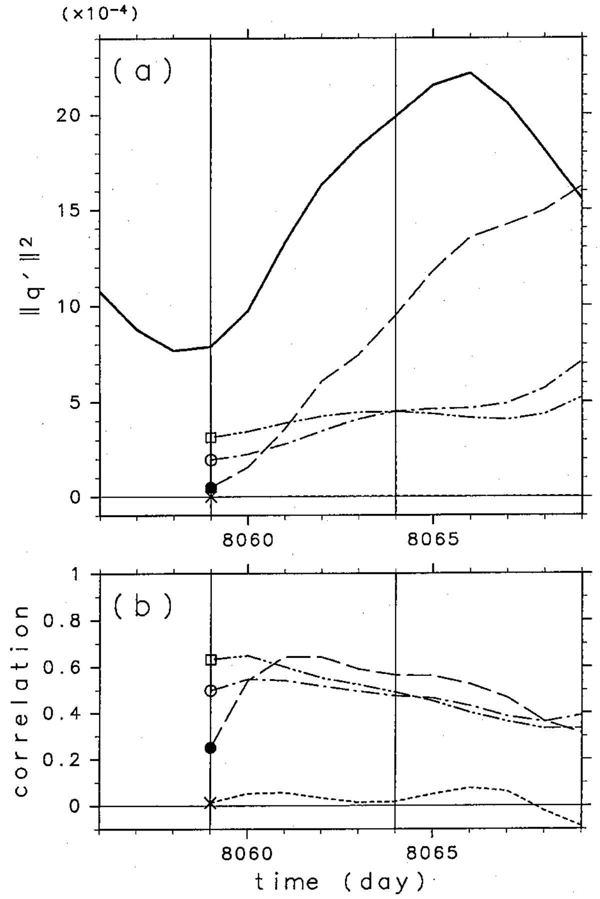

Fig. 11. (a) Temporal variations of the global mean enstrophy of disturbances. A solid line indicates the vorticity disturbance $\|q'(t)\|^2$ of the nonlinear solution for the period of Day 8056–8069. The other lines indicate the linear evolution of the projection of q'_I onto the space spanned by the unstable eigenmode, that is, the first 2 eigenvectors $\|\xi(t)\|^2$ (open circle and dot-dashed line), by the first 5 eigenvectors (square and dot-dot-dashed line), by the first optimal mode (cross and short-dashed line), and by the first 5 optimal modes $\|\zeta(t)\|^2$ (closed circle and long-dashed line). (b) Temporal variations of the coefficient of correlation between $q'(\lambda, \mu, t)$ and each linear evolution from Day 8059. Lines and markers are the same as those indicated in (a).

4.2 Linear responses to isolated initial perturbations

Responses of the time-averaged basic state to isolated initial perturbations were investigated using the linearized barotropic model. The spatial distribution of the initial vorticity perturbation was given by Gaussian form;

$$\eta(\lambda, \mu, t = \text{Day } 0) = B_0 \exp\left(-\frac{r^2(\lambda, \phi)}{2r_0^2}\right) + C_0, \quad (5)$$

where $r(\lambda, \phi)$ is an angular distance($0^\circ \le r \le 180^\circ$) between a point (λ, ϕ) and the center of Gaussian distribution, (λ_0, ϕ_0), which satisfies the relation $\cos r(\lambda, \phi) = \sin\phi \sin\phi_0 + \cos\phi \cos\phi_0 \cos(\lambda - \lambda_0)$. The amplitude B_0 of the distribution may be arbitrary in the linear evolution. The constant C_0 was set in order that the integration value of the vorticity perturbation η over the globe was zero. The 72 × 35 initial perturbations for $r_0 = 5^\circ$ and $B_0 = -1$ with the center (λ_0, ϕ_0) varied with intervals of 5° were evolved for 5 days with the barotropic model linearized about the time-averaged basic state. The amplification rate of the vorticity of the initial perturbation for a time interval τ, $\gamma(\tau) \equiv \|\eta(\tau)\|/\|\eta(0)\|$, was calculated for each linear evolution $\eta(t)$. The dependence of the amplification rate $\gamma(\tau)$ on the center (λ_0, ϕ_0) in the Northern Hemisphere is shown in Fig. 12 for $\tau = 1$ day (a), 3 days (b), and 5 days (c). As the time interval τ increases, the difference in the amplification rate of individual evolutions becomes larger. For these time intervals, the initial perturbations located upstream and equatorward of the jet maximum (see Fig. 5b) grow more rapidly than the initial perturbations of the other positions. On the contrary, some of the initial perturbations, for example $(\lambda_0, \phi_0) = (135^\circ, 15^\circ\text{N})$, continue to decay for 5 days in spite of the barotropically unstable basic state. All of the isolated initial vorticity perturbations whose center (λ_0, ϕ_0) is in the Southern Hemisphere decay ($\gamma(\tau) < 1$) for $\tau = 3$ days and 5 days.

The linear evolution of the initial vorticity perturbation for $(\lambda_0, \phi_0) = (210^\circ, 25^\circ\text{N})$ denoted by a marker + in Fig. 12b, which is the position of a local maximum of $\gamma(\tau = 3 \text{ days})$, is shown in Fig. 13 for Day $0 \le t \le$ Day 5. The spatial distribution of the initial vorticity perturbation $\eta(t = \text{Day } 0)$ (a) is localized upstream and equatorward of the jet maximum. The initially negative vorticity perturbation makes a positive vorticity perturbation with a large amplitude in the northeast (b) and a negative vorticity perturbation further downstream (c), and they organize themselves as a wave train on the waveguide of large $|\nabla\bar{q}|$ shaded in Fig. 5e. Further downstream developments of wave trains are seen in (d)–(f) with the indication of eastward propagation of energy at a higher speed than the phase propagation, consistent with the Rossby wave propagation. The temporal variation of the vorticity perturbation in the Western Hemisphere shown in Figs. 13c–13f resembles that of q' shown in Figs. 9c–9f. The amplification rates of this initial perturbation are $\gamma(\tau = 3 \text{ days}) = 1.77$ and $\gamma(\tau = 5 \text{ days}) = 2.31$, which are much larger than those of the unstable eigenmode perturbation shown in Fig. 10 [$\gamma(\tau = 3 \text{ days}) = 1.33$ and $\gamma(\tau = 5 \text{ days}) = 1.52$].

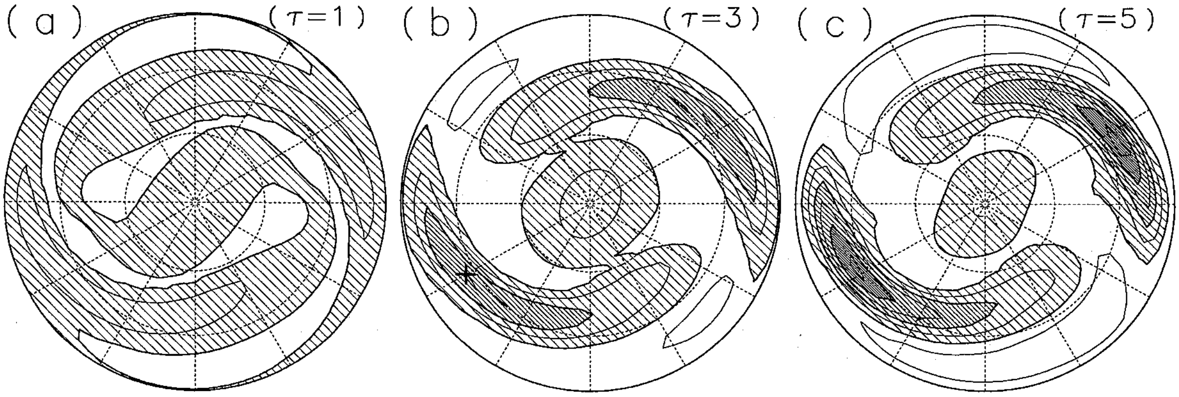

Fig. 12. Dependence of the amplification rate $\gamma(\tau)$ of isolated initial vorticity perturbation on its center of Gaussian distribution, (λ_0, ϕ_0). The time interval τ is, respectively, (a) 1 day, (b) 3 days, and (c) 5 days. Contour interval is 0.25 and shading indicates the region of amplification ($\gamma > 1$). A marker + in (b) denotes the position of a local maximum of $\gamma(\tau = 3$ days).

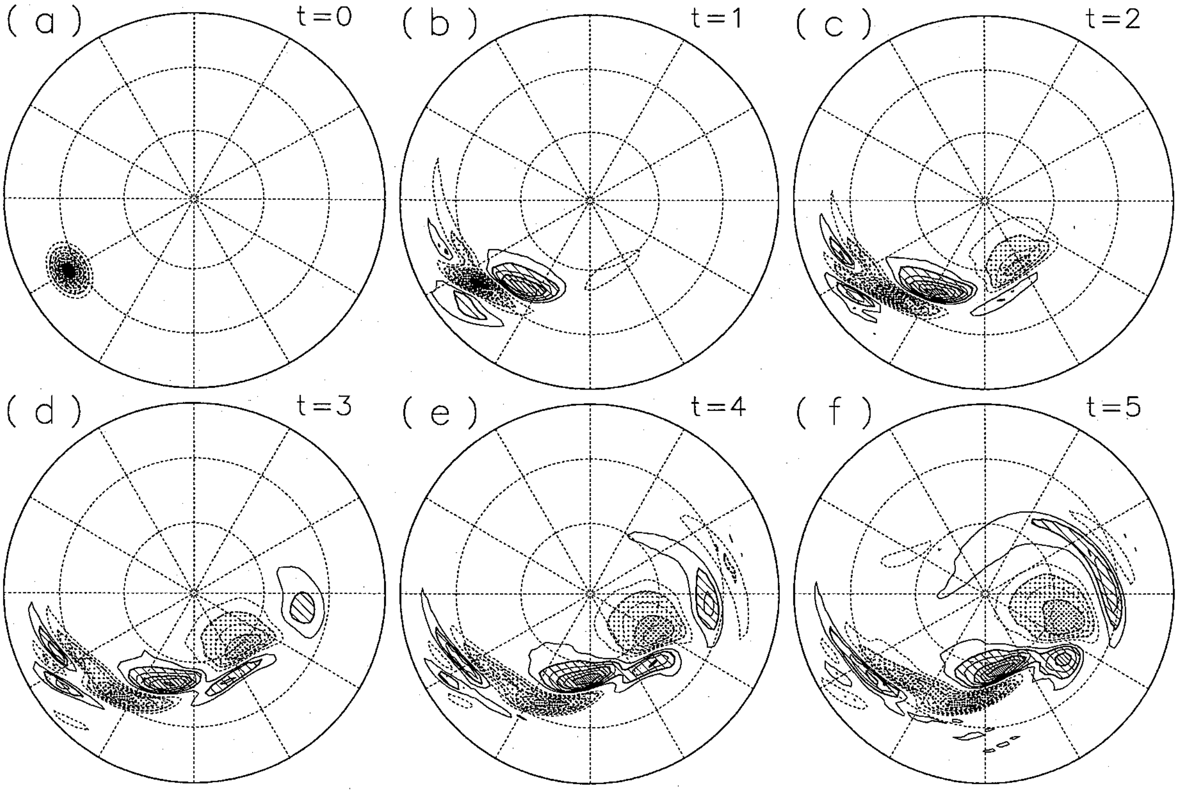

Fig. 13. Linear evolution of the vorticity perturbation $\eta(t)$ whose initial value is given by Eq. (1) for $(\lambda_0, \phi_0) = (210°, 25°\text{N})$, which is denoted by a marker + in Fig. 12b. Contour interval is 0.1 and shading indicates the region greater than 0.2 or less than −0.2. Zero-contours are omitted.

4.3 Optimal modes of the time-averaged field

The spatial distribution of the initial vorticity perturbation that grows most rapidly for a prescribed time interval was given by the first mode of the optimal excitation problem. We investigated optimal modes of the time-averaged basic state with the enstrophy norm; letting $\zeta(\lambda, \mu)$ be the vorticity of a perturbation, and with a measure of the perturbation as $||\zeta||$. The scientific methodologies of the optimal excitation problem are described in some papers, notably in Farrell (1988, 1989), and Lacarra and Talagrand (1988). As the optimal excitation problem deals with the growth of perturbations for a prescribed finite time-interval, the set of the optimal modes depends not only on the basic state but also on the time interval and the choice of norm that

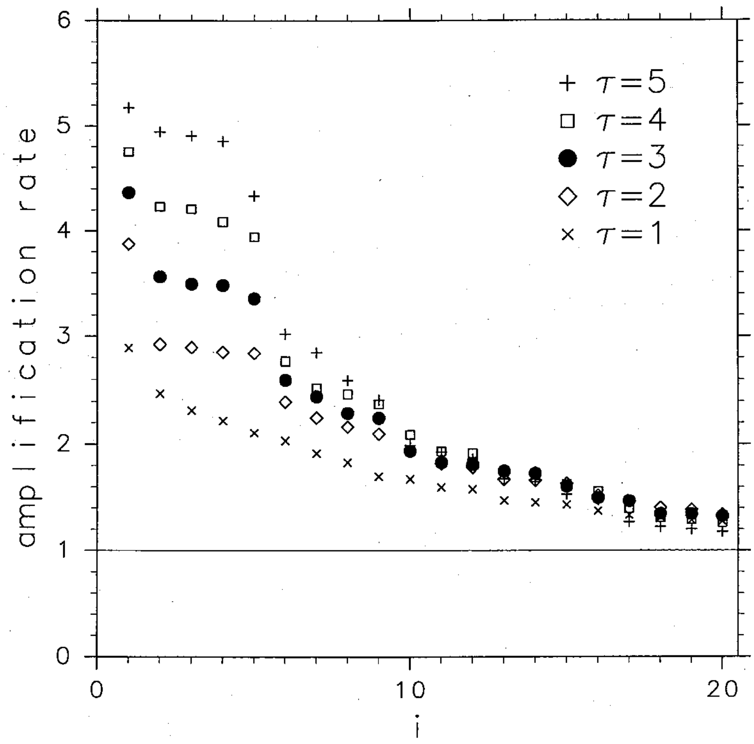

Fig. 14. The amplification rate $\gamma(\tau)$ of the first 20 optimal modes for five time intervals τ = 1-5 days.

measures the perturbation.

Figure 14 shows the amplification rate $\gamma(\tau)$ of the first 20 optimal modes for five time intervals from τ = 1 day to 5 days. All of the 20 optimal modes grow for these time intervals as $\gamma(\tau) > 1$. In the case of τ = 3 days, 44 modes grow and the remaining 1804 modes decay. As the time interval τ increases, the number of the growing modes decreases, which converges to the number of the dimension of the space spanned by the unstable eigenmode, 2, as τ increases to infinity. For $\tau = 2 \sim 5$ days, there is a significant difference in the amplification rate between the first 5 optimal modes and the 6th optimal mode. Moreover, the first 5 optimal modes can be also divided into two; *i.e.*, the 1st mode and next 4 modes for $\tau = 2 \sim 4$ days.

Figure 15 shows the vorticity distribution of the first 5 optimal modes $b_{i=1\sim5}(\lambda, \mu, t = \text{Day } 0)$ for τ = 3 days (upper panels) and the vorticity distribution of the perturbation evolved from the optimal mode for τ with the linearized model $b_{i=1\sim5}(\lambda, \mu, t = \tau)$ (lower panels). The first optimal mode $b_1(0)$ in (a) has small amplitudes in the wide area of high- and mid-latitudes, while the evolved perturbation $b_1(\tau)$ has large amplitudes locally in low-latitudes. The second optimal mode $b_2(0)$ in (b) has large amplitudes upstream and equatorward of the jet maximum, and is tilted against the shear of the jet. The evolved perturbation from the second optimal mode, $b_2(\tau)$, shows wavy perturbations on the waveguide of large $|\nabla\bar{q}|$. The third to the fifth optimal modes $b_{3\sim5}(0)$ in (c∼e) are similar to the second optimal mode $b_2(0)$ in the growth rate and the characteristics of the spatial structure. However, there is an essential difference between the four modes $b_{2\sim5}(0)$ in the phase of the wavy perturbations; the second $b_2(0)$ and the third $b_3(0)$ optimal modes are about $\pi/4$ out of phase for wavy perturbations, so are the fourth $b_4(0)$ and the fifth $b_5(0)$ optimal modes. Moreover, the second $b_2(0)$ and the fifth $b_5(0)$ optimal modes are about in phase in the Eastern Hemisphere and somewhat out of phase in the Western Hemisphere, and a similar relationship exists for the third $b_3(0)$ and the fourth $b_4(0)$ modes. The evolved perturbations of these four modes $b_{2\sim5}(\tau)$ have similar spatial patterns with large amplitude wave trains along the two waveguides.

In much the same way we determined the initial vorticity of the eigenmode perturbation, ξ_0, the initial vorticity of the optimal mode perturbation, $\zeta_0 \equiv \zeta(\lambda, \mu, t = \text{Day } 0)$, is determined by the projection of q'_{I} onto the space spanned by the first 5 optimal modes $b_{1\sim5}(0)$ for τ = 3 days. The coefficient of correlation $C(q'_{\text{I}}, \zeta_0)$ is 0.25, which is about half of $C(q'_{\text{I}}, \xi_0)$. The linear evolution of this optimal mode vorticity perturbation $\zeta(\lambda, \mu, t)$ is shown in Fig. 16 for Day $0 \le t \le$ Day 5. The initial vorticity perturbation ζ_0 in (a) shows a spatial distribution localized upstream and equatorward of the jet maximum with a tilt against the shear of the jet, similar to that of

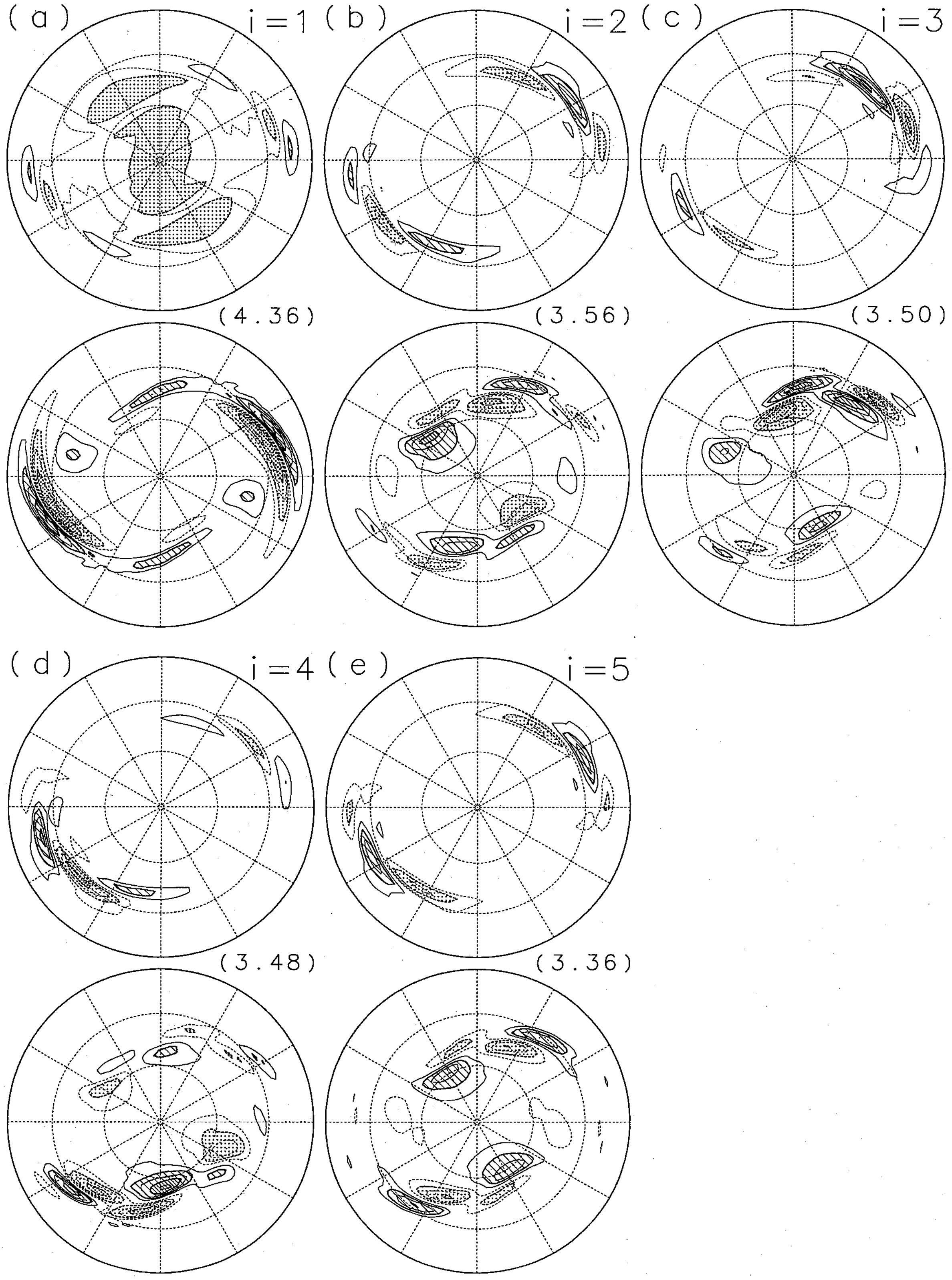

Fig. 15. Vorticity distribution of the first 5 optimal modes $b_{i=1\sim5}(\lambda, \mu, t = 0)$ for $\tau = 3$ days (upper panels) and vorticity distribution of the perturbation evolved from the optimal mode for τ, $b_{i=1\sim5}(\lambda, \mu, t = \tau)$ (lower panels). The value in the parentheses indicates the amplification rate $\gamma_i(\tau) = \|b_i(\tau)\|/\|b_i(0)\|$. Contour interval of the upper panels is, respectively, (a) 1 and (b)–(e) 2. Contour interval of the lower panels is 5. Shading of the upper panels indicates the region (a) < -2 or > 2, and (b)–(e) < -4 or > 4. Shading of the lower panels indicates the region < -10 or > 10. Zero-contours are omitted.

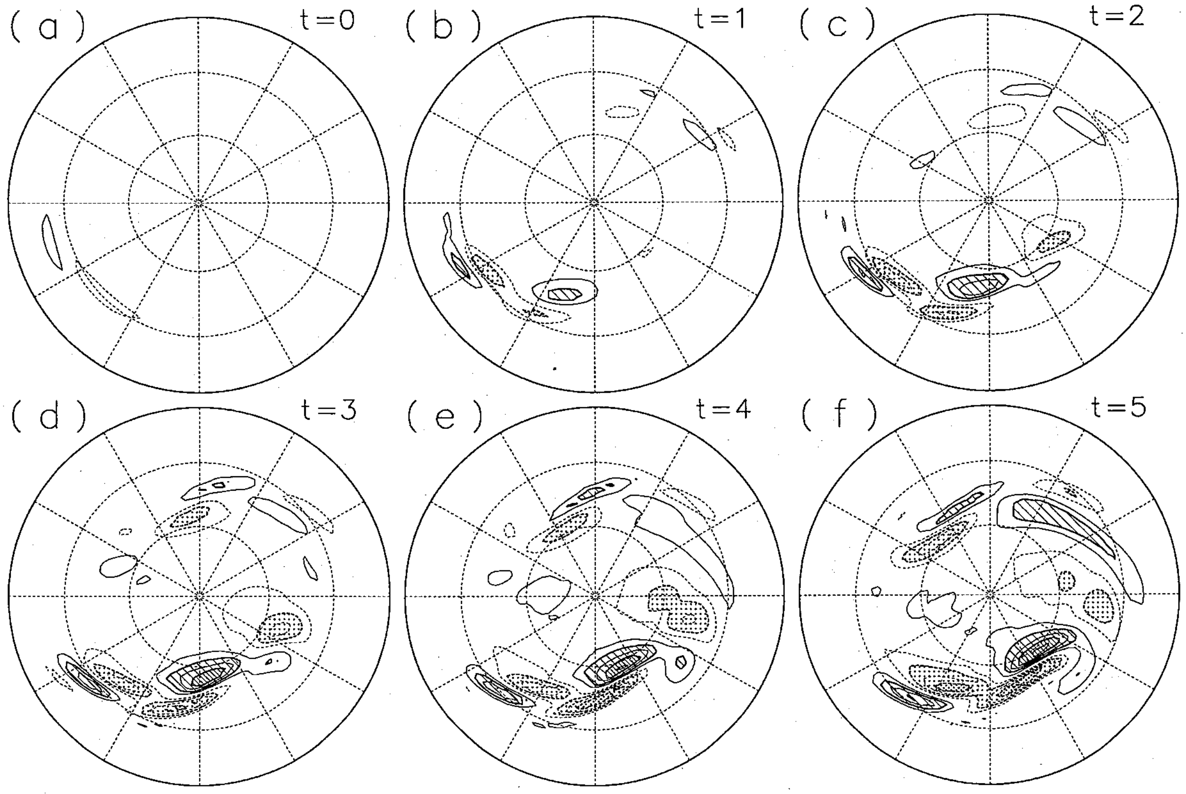

Fig. 16. Linear evolution of the optimal mode vorticity perturbation $\zeta(t)$ for the period of $0 \leq t \leq 5$. Contour interval and shading are same as those in Fig. 9.

the four optimal modes $b_{2\sim5}(0)$ shown in Figs. 15b–15e. In fact, the coefficient of correlation between the first optimal mode $b_1(0)$ and q'_{I}, $C(q'_{\mathrm{I}}, b_1(0))$, is only -0.013; the contribution of the the first optimal mode to ζ_0 is very small. Compared with the vorticity disturbance $q'(\lambda, \mu, t)$ shown in Fig. 9, the optimal mode vorticity perturbation $\zeta(\lambda, \mu, t)$ shows a very similar variation in the Western Hemisphere and successfully reproduces the rapid growth of the vorticity disturbances $q'(\lambda, \mu, t)$ for the period of Day 8059–8064.

In the same way as the eigenmode perturbation, the temporal variation of the global mean enstrophy of the optimal mode perturbation, $\|\zeta(t)\|^2$, is shown in Fig. 11a with a long-dashed line. Though the magnitude of the initial projection $\|\zeta_0\|^2$ (marked by a closed circle) is smaller than that of the eigenmode $\|\xi_0\|^2$ (marked by an open circle), $\|\zeta(t)\|^2$ grows very rapidly for the initial 3 days to exceed $\|\xi(t)\|^2$ and keep growing afterward. The increment of $\|\zeta(t)\|^2$ in the analysis period denoted by two vertical solid lines is as large as the increment of $\|q'(t)\|^2$. Note that the increment of enstrophy of the perturbation depends not only on its amplification rate but also on its initial magnitude. The coefficient of correlation $C(q'(t), \zeta(t - 8059 \text{ days}))$ denoted by a long-dashed line in Fig. 11b increases for the initial days and also exceeds $C(q'(t), \xi(t - 8059 \text{ days}))$ denoted by the dot-dashed line. Judging from the increment of the enstrophy for the period and the coefficient of correlation at Day 8064, the rapid growth of $q'(\lambda, \mu, t)$ is quantitatively described by the optimal mode vorticity perturbation $\zeta(\lambda, \mu, t)$ better than by the eigenmode vorticity perturbation $\xi(\lambda, \mu, t)$. A short-dashed line in Fig. 11 corresponds to the case of the projection onto the first optimal mode $b_1(0)$. Since the initial value marked by a cross is very small, there are no large increments in (a) and no large correlations in (b), in spite of its large amplification rate. Thus, the first optimal mode is not important for the rapid growth of q' for the period of Day 8059–8064 because of the small projection in the initial state.

4.4 Propagation of Rossby waves

Propagation of Rossby waves along the waveguide is diagnosed by using the wave activity M and wave activity flux $\boldsymbol{M}_{\mathrm{T}}$ introduced by Plumb (1986). Though he has derived a conservation law for three-dimensional propagation of transient eddies on a slowly varying time-mean flow, we reduced it into a two-dimensional form appropriate to the present model:

$$\frac{\partial M}{\partial t} + \nabla \cdot \boldsymbol{M}_{\mathrm{T}} = S_{\mathrm{M}}, \tag{6}$$

where

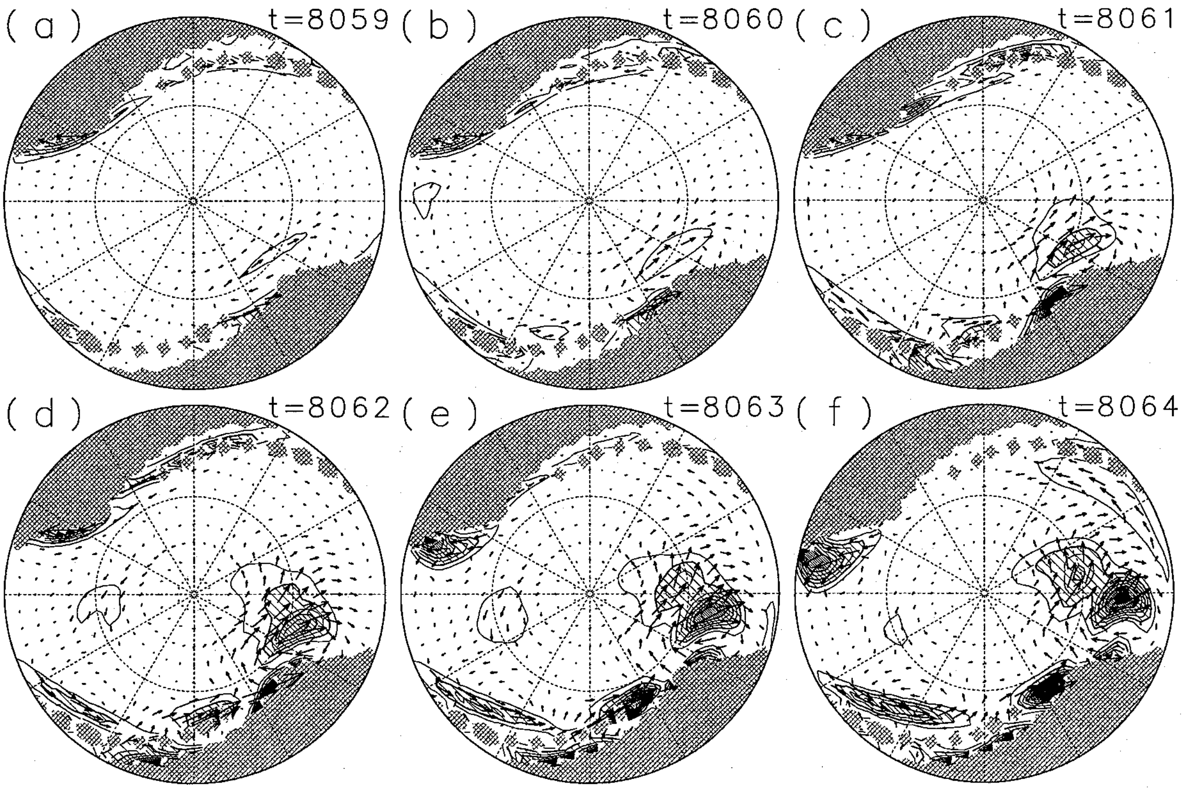

Fig. 17. Wave activity M (contours) and wave activity flux $\boldsymbol{M}_{\mathrm{T}}$ (arrows) for the same period as that in Fig. 8, Day 8059–8064. The outer circle of each map is 30°N. Areas where $|\nabla\bar{q}| < 0.5\cos\phi$ are hatched. Contour interval is 0.002 and shading indicates the region greater than 0.004.

$$M = \frac{q'^2\cos\phi}{2|\nabla\bar{q}|},$$

$$\boldsymbol{M}_{\mathrm{T}} = \boldsymbol{M}_{\mathrm{R}} + \bar{\boldsymbol{u}}M,$$

$$\boldsymbol{M}_{\mathrm{R}} = \mathsf{B}\boldsymbol{n},$$

$$\mathsf{B} = \cos\phi\begin{pmatrix} u'v' & (v'^2 - u'^2)/2 \\ (v'^2 - u'^2)/2 & -u'v' \end{pmatrix},$$

$$\boldsymbol{n} = \frac{\nabla\bar{q}}{|\nabla\bar{q}|},$$

and S_{M} represents sinks of wave activity, that is related with the dissipative terms of the right-hand side of Eq. (1) in our model.

Figure 17 shows the wave activity M and the wave activity flux $\boldsymbol{M}_{\mathrm{T}}$ for the period of Day 8059–8064; note that the plots are for $\phi \geq 30°\mathrm{N}$, and areas where $|\nabla\bar{q}| < 0.5\cos\phi$ are also hatched because the assumption used in the derivation of Eq. (6)-that the direction $\boldsymbol{n}$ is slowly varying on the sphere as compared with B-is not fully satisfied, especially not around the locally unstable areas. In the Western Hemisphere, a local maximum of the wave activity with an elliptic shape is observed around (330°, 60°N) at Day 8059 (a), which corresponds to the negative vorticity disturbance shown in Fig. 9a. This local wave activity amplifies and deforms into a more circular shape while moving southeastward slowly (b–d). A new wave activity separates from the dominant original and moves eastward (d–f). The dominant wave activity flux is roughly parallel to the waveguide; eastward for longitudes 300 ∼ 330° and south-eastward for 330 ∼ 360°. A great increase of the wave activity occurs during this period around the jet exit region, where $|\nabla\bar{q}|$ becomes small as shown in Figs. 5b and 5e. A large convergence of the wave activity flux is observed in the southeast of the wave activity, which is consistent with the propagation and amplification of the wave activity. Propagation of Rossby waves in a zonally varying basic state plays an important role in the amplification of vorticity disturbance around the jet exit region. However, the wave activity is not a very useful diagnostic tool for large disturbances in the other areas, because the amplification of these disturbances is closely related with the local instability of the time-averaged state.

5. Discussion

In the previous section, a typical example of the rapid growth of vorticity disturbances, which occurs irregularly and intermittently in the nonlinear solution described in Subsection 3.1, was throughly examined from four different dynamical viewpoints;

eigenmodes of the time-averaged field, linear responses to isolated initial perturbations, optimal modes of the time-averaged field, and propagation of Rossby waves. The growth of disturbances can be predicted roughly by a measure of the disturbances projected onto a small number of optimal modes; a dashed curve in Fig. 7 shows the temporal variation of the projection onto the space spanned by the first 5 optimal modes for $\tau = 3$ days, while a thick solid curve is the temporal variation of the measure of the disturbance $\|q'\|$. The projection becomes large before $\|q'\|$ becomes large. The cross-correlation function between the two curves based on the 10,000-day dataset has a maximum 0.77 at 4-day lag and 0.75 at 3-day lag. The same calculation with the projection onto the space spanned by 4 optimal modes from the second to the fifth shows similar results of a maximum correlation 0.78 at 4-day lag and 0.74 at 3-day lag. It is surprising that such a high correlation is obtained from the projection only with the 4 optimal modes. The same calculation with the first 4 optimal modes for $\tau = 3$ days based on the energy norm $\|\nabla\psi'\|$ shows a maximum correlation 0.61 at 3-day lag, where the first 4 energy optimal modes have similar growth rate and spatial structure as have the 4 enstrophy optimal modes from the second to the fifth. The difference of the correlation indicates that the optimal modes with the enstrophy norm predict the growth of disturbance in the present example better than those with the energy norm. The difference seems to be related to the fact that the number of the growing energy optimal-modes (191) is much larger than that of the growing enstrophy optimal-modes (44) for $\tau = 3$ days.

In dealing with the optimal mode, it is necessary to determine the norm that measures the disturbances. Although the energy norm has been used in most of the studies of the optimal excitation problem (*e.g.*, Borges and Hartmann, 1992; Sardeshmukh *et al.*, 1997), the enstrophy norm was adopted in this study because of the high value of the cross-correlation stated previously. By using the energy norm it has been shown that the first optimal mode of the climatological mean flow in the upper troposphere has a large amplitude upstream and equatorward of the African-Asian jet maximum and is strongly tilted against the shear of the jet (*e.g.*, Borges and Hartmann, 1992; Sardeshmukh *et al.*, 1997). An explanation of this structure was given by the fact that in a linear shear flow the disturbances with phase lines tilted against the shear may increase their energy for a finite time interval without substantial increase of their enstrophy (Orr, 1907; Boyd, 1983; Shepherd, 1985). However, this mechanism should not be essential in the present optimal excitation problem with the enstrophy norm. Nonetheless, the enstrophy optimal modes obtained in our model as the 2–5th modes show the structure that has large amplitude upstream and equatorward of the jet maximum and is tilted against the shear (the upper panels in Figs. 15b–15e), which is very similar to the structure of the optimal modes with the energy norm. Therefore, another mechanism for the rapid growth of such disturbances is required to explain the substantial increase of the enstrophy.

The structure of rapidly growing disturbances is well described by the optimal modes of the time-averaged field in other chaotic solutions around the previous example for $\rho = 0.180$. This is also true for the periodic solution for $\rho = 0.140$; spatial patterns of rapidly growing disturbances in the periodic solution are very similar to those for $\rho = 0.180$ shown in Fig. 9. The unstable eigenmode of the time-averaged field for the periodic solution also has a similar spatial pattern to that for $\rho = 0.180$ shown in Fig. 10, while both the e-folding time (27.6 days) and period (27.7 days) of the unstable eigenmode for $\rho = 0.140$ are longer than those for $\rho = 0.180$. Thus it is difficult to explain the nonlinear variations of the periodic solution for $\rho = 0.140$ with the unstable eigenmode of the time-averaged field.

One might oppose the comparison between the first 5 optimal modes and only the unstable eigenmode associated with the first 2 eigenvectors. Squares and dot-dot-dashed lines in Fig. 11 represent the case of the projection onto the 5-dimensional space spanned by the first 5 eigenvectors obtained by the eigenanalysis. The first 5 eigenvectors consist of the unstable eigenmode described in Subsection 4.1 and two stable eigenmodes associated with one pair of complex eigenvalues whose $1/e$-time is 39.8 days and period is 10.6 days and with one real eigenvalue whose $1/e$-time is 37.5 days. Although the magnitude of the initial projection for the first 5 eigenvectors, which is marked by the squares in Fig. 11, is larger than that for the first 2 eigenvectors, marked by the open circles, both the global mean enstrophy and the coefficient of correlation to $q'(\lambda, \mu, t)$ of the vorticity perturbation for the first 5 eigenvectors are almost the same as those for the first 2 eigenvectors after 5 days. As to the increment of the enstrophy for the period, it is smaller than that for the first 2 eigenvectors. Hence the rapid growth of $\|q'(t)\|$ can not be explained by the eigenmodes even if the number of eigenmodes is increased as the same number of the optimal modes we adopted.

The dependence of the stability of a zonally varying basic state on the topography, which Andrews (1984) pointed out, can be examined in our model. The topographic term was included in the linear stability analysis in Subsection 4.1. Here, eigenvalues of Jacobian matrix without the topographic term assuming $\bar{q} = \rho\Delta\bar{\psi} + \mu$ were calculated and only unstable modes are listed at the bottom of Table 1. There are two pairs of complex eigenvalues with a positive real part. The most unstable one in the present no topography case has the e-folding time of 30.5 days, which is roughly twofold of that in the original case with topography, although the period and spatial pattern are similar. The barotropic instability of the zonally varying time-averaged state is underestimated in our model, if the topographic term is disregarded.

We have investigated the relation between the irregular fluctuation and the time-averaged field using a simple barotropic model. Chaotic solutions obtained in the present model do not show any hint of multiple flow regimes and are characterized by variations around the time mean. This is the reason why the present linear analysis is useful to understand the nonlinear variations. On the other hand, transitions between some flow regimes, *e.g.*, a blocking regime and a zonal regime, are observed in the real atmosphere and in some numerical models (*e.g.*, Itoh and Kimoto, 1996). In such systems with multiple flow regimes, the time mean field may not be very useful for the linear analyses; a mean state of each regime could be more useful.

6. Conclusions

Fundamental dynamics of extra-tropical low-frequency variations were examined by numerical experiments based on a simple barotropic model with topography, which is a forced-dissipative autonomous system. Asymptotic solutions of the model for realistic parameter ranges showed irregular variations with a dominant period of $10 \sim 20$ days (Fig. 3). The time-averaged state revealed a zonal variation under the influence of the topography (Fig. 5), as did the climatological mean state in the upper troposphere. Low-frequency variations obtained in the present nonlinear model were characterized by the rapid growth of disturbances that took place intermittently and irregularly. The growing disturbances showed wave train patterns along the waveguides where $|\nabla\bar{q}|$ is large (Fig. 9).

In order to understand the mechanism of such rapid growth of disturbances, linear characteristics of the time-averaged basic state, such as eigenmodes, optimal modes, and linear responses to isolated initial perturbations, were investigated. Compared with the eigenmodes and the optimal modes, the rapid growth was reasonably explained by the linear evolution of the optimal modes (Fig. 16) rather than that of the unstable eigenmode (Fig. 10). The optimal modes had wave-like structures that were highly localized upstream and equatorward of the jet maximum and were tilted against the shear (the upper panels in Figs. 15b–15e). Evolution of the optimal modes showed wave trains along the waveguide. The results of the linear responses of isolated initial perturbations also indicated that the areas upstream and equatorward of the jet maximum were favorable for the rapid growth of the perturbations (Fig. 12), and their linear evolution also shows wave train patterns along the waveguide (Fig. 13), which are similar to those seen in the nonlinear model and the optimal modes. The diagnosis with the wave activity and the wave activity flux introduced by Plumb (1986) indicated that the propagation of Rossby waves plays an important role in the amplification of the vorticity disturbance around the jet exit region observed in the nonlinear model (Fig. 17).

Acknowledgments

We thank Dr. K. Ishioka for his FORTRAN package of the barotropic model with the spectral transform method in the spherical domain. GFD-DENNOU Library was used for drawing the figures. Numerical calculation was done on the KDK system at Radio Atmospheric Science Center, Kyoto University and VPP500/15 at Data Processing Center, Kyoto University. This work was supported in part by the Grant-in-Aid for Scientific Research of the Ministry of Education, Science, Sports and Culture of Japan, and by the Grant-in-Aid for the Cooperative Research with Center for Climate System Research, University of Tokyo.

References

Andrews, D.G., 1984: On the stability of forced nonzonal flows. *Quart. J. Roy. Meteor. Soc.*, **110**, 657–662.

Borges, M.D. and D.L. Hartmann, 1992: Barotropic instability and optimal perturbations of observed nonzero flows. *J. Atmos. Sci.*, **49**, 335–354.

Borges, M.D. and P.D. Sardeshmukh, 1995: Barotropic Rossby wave dynamics of zonally varying upper-level flows during northern winter. *J. Atmos. Sci.*, **52**, 3779–3796.

Boyd, J.P., 1983: The continuous spectrum of linear Couette flow with the beta effect. *J. Atmos. Sci.*, **40**, 2304–2308.

Branstator, G. and I. Held, 1995: Westward propagating normal modes in the presence of stationary background waves. *J. Atmos. Sci.*, **52**, 247–262.

Charney, J.G. and J.G. DeVore, 1979: Multiple flow equilibria in the atmosphere and blocking. *J. Atmos. Sci.*, **36**, 1205–1216.

Farrell, B.F., 1988: Optimal excitation of neutral Rossby waves. *J. Atmos. Sci.*, **45**, 163–172

Farrell, B.F., 1989: Optimal excitation of baroclinic waves. *J. Atmos. Sci.*, **46**, 1193–1206.

Hoskins, B.J. and T. Ambrizzi, 1993: Rossby wave propagation on a realistic longitudinally varying flow. *J. Atmos. Sci.*, **50**, 1661–1671.

Huang, H-P. and W.A. Robinson, 1995: Barotropic model simulations of the North Pacific retrograde disturbances. *J. Atmos. Sci.*, **52**, 1630–1641.

Itoh, H. and M. Kimoto, 1996: Multiple attractors and chaotic itinerancy in a quasigeostrophic model with realistic topography: implications for weather regimes and low-frequency variability. *J. Atmos. Sci.*, **53**, 2217–2231.

Kubǐcek, M. and M. Marek, 1983: *Computational Methods in Bifurcation Theory and Dissipative Structures.* Springer-Verlag, 243pp.

Lacarra, J. and O. Talagrand, 1988: Short-range evolution of small perturbations in a barotropic model. *Tellus*, **40A**, 81–95.

Legras, B. and M. Ghil, 1985: Persistent anomalies, blocking and variations in atmospheric predictability. *J. Atmos. Sci.*, **42**, 433–471.

Mukougawa, H. and T. Ikeda, 1994: Optimal excitation of baroclinic waves in the Eady model. *J. Meteor. Soc. Japan*, **72**, 499–513.

Naoe, H., Y. Matsuda and H. Nakamura, 1997: Rossby wave propagation in idealized and realistic zonally varying flows. *J. Meteor. Soc. Japan*, **75**, 687–700.

Newman, M., P.D. Sardeshmukh and C. Penland, 1997: Stochastic forcing of the wintertime extratropical flow. *J. Atmos. Sci.*, **54**, 435–455.

Orr, W.M'F., 1907: The stability or instability of the steady motions of a perfect liquid and of a viscous liquid. *Proc. Roy. Irish Acad.*, **A27**, 9–138.

Plumb, R.A., 1986: Three-dimensional propagation of transient quasi-geostrophic eddies and its relationship with the eddy forcing of the time-mean flow. *J. Atmos. Sci.*, **43**, 1657–1678.

Sardeshmukh, P.D., M. Newman and M.D. Borges, 1997: Free barotropic Rossby wave dynamics of the wintertime low-frequency flow. *J. Atmos. Sci.*, **54**, 5–23.

Shepherd, T.G., 1985: Time development of small disturbances to plane Couette flow. *J. Atmos. Sci.*, **42**, 1868–1871.

Simmons, A.J., J.M. Wallace and G.W. Branstator, 1983: Barotropic wave propagation and instability, and atmospheric teleconnection patterns. *J. Atmos. Sci.*, **40**, 1363–1392.

Swanson, K.L., P.J. Kushner and I.M. Held, 1997; Dynamics of barotropic storm tracks. *J. Atmos. Sci.*, **54**, 791–810.

Yang, G.-Y. and B.J. Hoskins, 1996: Propagation of Rossby waves of nonzero frequency. *J. Atmos. Sci.*, **53**, 2365–2378.

帯状非対称性のある簡略化した順圧モデルにおける長期変動と最適励起について

山根省三[1]・余田成男

（京都大学大学院理学研究科地球惑星科学専攻）

強制と散逸、地形の項を含む簡略化した球面順圧モデルを使った数値実験により、中・高緯度の長期変動の基本的な力学について研究を行った。このモデルの解は、現実的なパラメータ領域において長周期の不規則な変動を示す。その解の時間平均場は、上部対流圏の時間平均場がそうであるように、地形の影響を受けてジェットが帯状に変化する構造となっている。ジェット極大域の上流・赤道寄りは、擾乱(時間平均場からのずれ成分)の急激な成長に好都合な場所である。固有モードや最適モード、孤立した初期摂動の線型応答などの時間平均場の線型的な特性を詳しく調べて、非線型な非周期解の変動との比較を行った。その結果、非周期解に見られる擾乱の急激な成長は、不安定な固有モードというよりはむしろ最適モードの線型発展で良く説明されることが分かった。また、波活動度を用いた診断により、ロスビー波の伝播がジェットの出口付近での擾乱の成長にとって重要であることが分かった。

---

[1] 現所属：地球フロンティア研究システム